

Chapter 10

Computing Motion Dependent Afferent Activity During Cat Locomotion Using a Forward Dynamics Musculoskeletal Model

Boris I. Prilutsky, Alexander N. Klishko, Douglas J. Weber and Michel A. Lemay

Abstract The structure and function of mammalian locomotor central pattern generators (CPGs) and their control by afferent feedback *in vivo* are not completely understood. The aim of this study was to develop a forward dynamics model of cat hindlimbs that using neural or muscle activity as input generates realistic locomotion mechanics and motion-dependent afferent activity. This model can be combined with CPG models to study the spinal control of locomotion using a comprehensive closed-loop neuromechanical model. The developed planar, 10-DOF model of two cat hindlimbs with 18 Hill-type muscle actuators generated realistic walking mechanics and firing rates of muscle type Ia, Ib, II and paw pad cutaneous afferents matching experimental results. The afferent activities were obtained from computed muscle fiber length and velocity, tendon force and simplified relationships transforming these mechanical variables to the afferent firing rates. The computed afferent signals were consistent with their suggested role in triggering locomotor phase transitions.

Keywords Locomotion · Afferent activity · Forward dynamics · Computational modeling · Cat

B. I. Prilutsky (✉) · A. N. Klishko
School of Applied Physiology, Center for Human Movement Studies, Georgia Institute of Technology, 555 14th Street NW, Atlanta, GA 30332, USA
e-mail: boris.prlutsky@ap.gatech.edu

D. J. Weber
Department of Physical Medicine and Rehabilitation, Department of Bioengineering, University of Pittsburgh, Pittsburgh, PA, USA

M. A. Lemay
Department of Bioengineering, Temple University, 1947 N 12th St, Philadelphia, PA 19122, USA

© Springer Science+Business Media New York 2016

B. I. Prilutsky, D. H. Edwards (eds.), *Neuromechanical Modeling of Posture and Locomotion*, Springer Series in Computational Neuroscience, DOI 10.1007/978-1-4939-3267-2_10

10.1 Introduction

Mammalian locomotion is a complex motor behavior which involves sensorimotor integration at different levels of the central nervous system (Grillner 1981; Orlovsky et al. 1999; Rossignol 2006). A network of neural circuits in the lumbar region of the mammalian spinal cord, called central pattern generators (CPGs), is involved in generating hindlimb locomotor activity in quadrupedal mammals. The CPG can produce locomotor-like activity of hindlimb motoneurons and flexor and extensor muscles in the absence of descending rhythmic input (spinal cord transection at thoracic level; (Grillner 1981)) or proprioceptive feedback (deafferentation) in the cat (Brown 1914). In intact animals, CPG rhythmic activity is modulated by both descending commands (Shik et al. 1969; Grillner et al. 1999) and motion-dependent proprioceptive feedback (McCrea 2001; Pearson 2008).

The motion-dependent feedback from limb muscles and foot skin has been proposed to adjust CPG activity to the external environment and to regulate swing-stance and stance-swing transitions (McCrea 2001; Pearson 2008). Evidence for afferent regulation of mammalian CPG activity has been obtained in experiments performed in fictive locomotion preparations and on walking animals. In fictive locomotion preparations, neuromuscular transmission is blocked pharmacologically and CPG locomotor rhythm, recorded in muscle nerves and individual motoneurons and interneurons, can be elicited by electrical stimulation of the midbrain locomotor regions (Shik et al. 1969; Jordan 1998). During fictive locomotion, electrical stimulation of peripheral nerves exciting the large group I afferents (Ia, muscle length and velocity sensitive, and Ib, muscle force sensitive) of the ankle extensors enhances extensor activity in most extensor hindlimb muscle nerves if delivered during the extensor phase and resets the phase to extensor if delivered during the flexor phase (Conway et al. 1987; Guertin et al. 1995). Similar stimulations in walking animals during the stance phase enhances extensor activity (Pearson and Collins 1993; Whelan et al. 1995) as does stimulation of the cutaneous afferents innervating plantar surface of the foot (Duysens and Loeb 1980).

Although it is clear that afferent regulation of CPG activity during mammalian locomotion takes place, the detailed mechanisms of such regulation are still elusive. It is because the structure of the mammalian CPG networks and its elements receiving afferent feedback and supraspinal inputs has not been identified (McCrea and Rybak 2008; Kiehn 2011). In addition, it is impossible to distinguish effects of electrical stimulation of muscle length-velocity sensitive Ia and muscle force sensitive Ib afferents on the CPG activity because these afferents have similar excitation thresholds. Recent studies in transgenic mice without functioning spindle afferents or Golgi tendon organs revealed differential roles of these afferents during mammalian locomotion (Akay et al. 2014; Takeoka et al. 2014). Since in the above studies proprioceptive feedback in the transgenic mice was removed from all muscles, the contribution of spindle and Golgi tendon organ afferents from specific muscles to regulation of CPG activity is still unknown.

One approach to addressing this and other issues of the CPG control of mammalian locomotion is neuromechanical modeling and computer simulations. Several

models of terrestrial locomotor CPGs integrated with a biomechanical system through motion-dependent feedback have been developed and analyzed (He et al. 1991; Ivashko et al. 2003; Yakovenko et al. 2004; Ekeberg and Pearson 2005; Markin et al. 2010; Aoi et al. 2013; see also Chapters by Aoi 2015; Bondy et al. 2015; Markin et al. 2015 in this book). In most of these studies, however, either the CPG model did not reproduce the relevant experimental observations (e.g., changes in rhythmic motoneuronal activity during fictive locomotion as a result of afferent stimulation (Rybak et al. 2006b) or the musculoskeletal models did not include biomechanical details important for determining motion-dependent afferent input (e.g., the muscle series elastic element that affects muscle fascicle length changes during walking (Hoffer et al. 1989; Maas et al. 2009). For example, the model of cat hindlimb locomotion by (Ivashko et al. 2003) included a CPG controlling nine groups of motoneurons in each hindlimb that excited the corresponding Hill-type muscle actuators. The CPG activity was modulated by motion-dependent feedback signals from muscles and paw skin receptors. Although this model demonstrated stable locomotion with patterns of muscle activity, kinematics and ground reaction forces somewhat similar to real cat locomotion, it had a number of limitations. Specifically, the CPG model was not based on and did not reproduce experimental observations obtained in fictive locomotion (Rybak et al. 2006a, b). The musculoskeletal parameters of the cat hindlimb model were not optimized within physiologically reasonable ranges. As a result, the model could not quantitatively reproduce muscle responses to imposed muscle length changes, or joint kinematics, ground reaction forces and joint moments of the walking cat when recorded muscle activity was used as input to the model. Furthermore, computed motion-dependent afferent signals were assumed proportional to muscle length, velocity, and force and did not reproduce nor were validated against the afferent signals recorded during locomotion. It is expected that in muscles with a relatively long tendon a substantial part of the muscle-tendon unit stretch can be taken up by the stretched tendon reducing elongation of muscle fibers and thus the output from length and stretch velocity sensitive spindle afferents (Hoffer et al. 1989; Maas et al. 2009). Therefore to accurately predict length- and velocity-dependent sensory feedback, the tendon elasticity must be incorporated in the model. Accurate tendon force estimation in individual muscle-tendon units during locomotion is also necessary for realistic predictions of sensory feedback signals from Golgi tendon organs.

Our long-term goal of modeling the spinal locomotor control has been to develop a comprehensive neuromusculoskeletal model of mammalian locomotor system that integrates the CPG model reproducing fictive locomotion experiments (Rybak et al. 2006a, b) and a detailed musculoskeletal model of the cat hindlimbs reproducing muscle force responses, walking mechanics and motion-dependent afferent signals. Such an integrated neuromusculoskeletal model will serve as a common computational framework for studying neural control of locomotion in the intact and spinalized animals and the effects of afferent feedback on restoring spinal locomotion (for details see (Markin et al. 2015)).

The aim of this work was four-fold: (1) Develop a forward dynamics musculoskeletal model of the cat hindlimbs that generates the activity of spindle

(groups Ia, II), tendon organ (group Ib), and paw pad cutaneous afferents using neural or muscle EMG activity as input and computes muscle fiber length and velocity and tendon forces; (2) Validate simulated muscle force responses to imposed muscle length changes as well as mechanics of locomotion against the experimental joint angles, ground reaction forces, and joint moments; (3) Compare the computed muscle length- and force-dependent afferent signals with activity of selected afferents recorded during cat locomotion (Loeb and Duysens 1979; Loeb et al. 1985; Prochazka and Gorassini 1998a, b; Weber et al. 2007); and (4) Examine if computed proprioceptive signals were consistent with their suggested role in triggering locomotor phase transitions and modulating CPG activity. Our main hypothesis was that patterns of afferent activity during walking computed from the simulated muscle length and velocity, tendon force and ground reaction force applied to the paw would be similar to the patterns of afferent activity recorded during cat walking and reported in the literature.

Preliminary results of this work were published in an abstract form (Prilutsky and Klishko 2007; Prilutsky et al. 2013).

10.2 Model Development

The developed musculoskeletal model, although similar in some respects to several previously published models of cat hindlimbs (He et al. 1991; Ivashko et al. 2003; Yakovenko et al. 2004; Ekeberg and Pearson 2005; Markin et al. 2010; Bunderson et al. 2012; see also Chap. 1 by Bunderson and Bingham (2015) in this book) is unique because it incorporates all relevant model features that previously were not integrated in a single model. Specifically, the model uses as input electromyographic (EMG) activity recorded intramuscularly in relevant hindlimb muscles. The equations of muscle dynamics incorporate such muscle properties as muscle mass, the force-length-velocity relations of the contractile element and the force-length relations of the tendon and the muscle parallel elastic elements. Many parameters of the musculoskeletal model (i.e., positions of origin and insertion of each muscle) were directly measured; then these and other parameters were tuned to obtain a close match between the experimental and simulated locomotion. In addition, model output included motion-dependent proprioceptive signals that are computed using regression equations relating afferent firing rates with muscle length and velocity, tendon force and muscle activation. These regression equations were developed based on *in vivo* recordings in walking cats (Prochazka and Gorassini 1998b; Prochazka 1999; Weber et al. 2007).

10.2.1 *Experimental Data for Model Development*

To ensure realistic simulations of cat hindlimb locomotor movements, parameters of the model were tuned to match as close as possible simulated and experimentally

obtained hindlimb mechanics. The developed model was tested by comparing computed activity patterns of muscle and paw pad afferents with those recorded experimentally during unrestrained walking in cats.

10.2.1.1 Recordings and Analysis of Muscle Activity and Walking Mechanics

To optimize tendon and muscle model parameters, we recorded EMG activity of 9 hindlimb muscles, muscle fascicle length and mechanics of walking in 5 adult cats (*Felis catus*) (mass 3.24 ± 0.40 kg) using experimental procedures consistent with US Public Health Service Policy on Humane Care and Use of Laboratory Animals and approved by the Institutional Animal Care and Use Committee of Georgia Institute of Technology (for details see (Gregor et al. 2006; Maas et al. 2009; Prilutsky et al. 2011)). Briefly, the animals were trained for 3–5 weeks to walk on a Plexiglas enclosed walkway (3.0 m \times 0.4 m) with 3 embedded force plates (0.16 m \times 0.11 m and 0.11 m \times 0.07 m; Bertec, USA) using food rewards. Mechanics of walking at self-selected speed were recorded using Vicon (UK) motion capture system and small reflective markers (6–9 mm in diameter) placed on hindlimbs' joints (Fig. 10.1a). After initial data collection, 9 pairs of thin Teflon-insulated multi-stranded stainless-steel wires (CW5402, Cooner Wire, USA) were implanted into 9 muscles of right hindlimb (Fig. 10.1c) under aseptic conditions and isoflurane anesthesia. The wires were attached to two multi-pin Amphenol connectors fixed to the skull by stainless steel screws and acrylic cement. After recovery (10–14 days), walking mechanics and muscle activity were collected for several weeks. No deviations from pre surgery walking patterns were noticed. Sampling rates were 120, 360, and 3000 Hz for kinematics, ground reaction forces and EMG, respectively. Marker displacements were low-pass filtered (5–6 Hz cutoff frequency, 4-order Butterworth zero-lag filter). Raw EMG signals were band-pass filtered (30–1500 Hz) and rectified. EMG bursts were identified by selecting a threshold EMG value (2 SD of the mean between-burst baseline activity) above which the muscle was considered active (Fig. 10.2a, SO); subsequently the baseline activity was set to zero. The modified rectified signals were low-pass filtered at 30 Hz, normalized to the EMG linear envelope maximum value across all cycles within the muscle and cat, and then averaged for each percent of the cycle time across all walking cycles of each cat and across 5 cats (Fig. 10.2b). Recorded or computed ground reaction forces, joint angles and joint moments (for details see (Gregor et al. 2006; Prilutsky et al. 2011)) were also averaged for each percent of the cycle time. After completion of data collection, the animal was euthanized with an overdose of pentobarbital sodium (120–180 mg/kg, intravenous administration). Immediately after euthanasia, both hindlimbs were dissected, placements of EMG electrodes were verified, and segment lengths and locations of origin and attachment midpoints of each muscle were measured using a caliper.

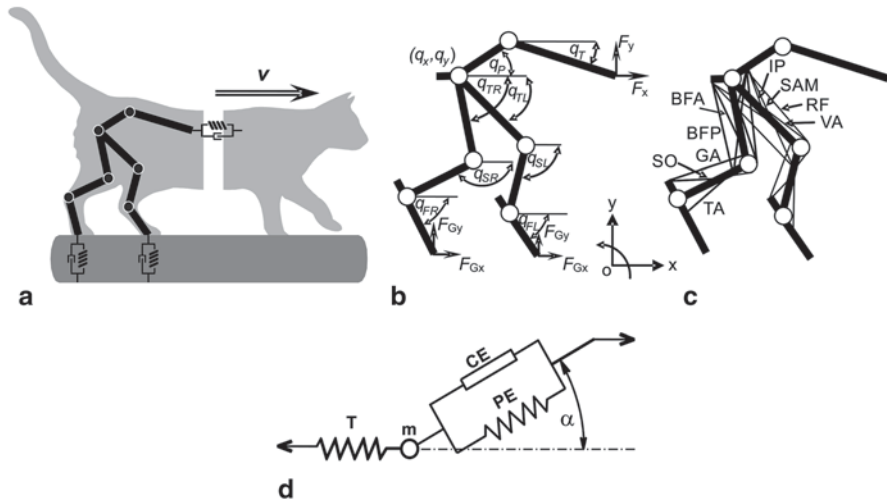


Fig. 10.1 Schematic representation of the musculoskeletal model of the cat hindlimbs. **a** The hindlimbs, pelvis and posterior trunk interacting with the ground and the anterior trunk, head and forelimbs. These interactions are modeled as viscoelastic forces. **b** A 10-DOF planar system of rigid segments with frictionless revolute joints representing two hindlimbs, pelvis and posterior trunk. Each hindlimb consists of the foot, shank, and thigh. Ten generalized coordinates describe kinematics of the system: hip horizontal and vertical coordinates and hindlimb segment angles with respect to the horizontal axis. Interactions of the feet and the trunk with external environment are simulated by viscoelastic horizontal and vertical forces (F_{Gx} , F_{Gy}) (see text for details). **c** Schematic representation of muscles of the model: *IP* iliopsoas, *BFA* biceps femoris anterior, *RF* rectus femoris, *BFP* biceps femoris posterior, *SAM* sartorius medial, *VA* vastii, *GA* gastrocnemii, *TA* tibialis anterior, and *SO* soleus. **d** A schematic representation of a Hill-type model of the muscle-tendon unit (MTU). *T* tendon, *m* muscle mass located at the muscle-tendon junction, *CE* the contractile element, *PE* the parallel elastic element and α angle of pennation

10.2.1.2 Recording and Analysis of Activity from Paw Cutaneous Afferents

The cutaneous afferent recordings used in this study were obtained on one day of recordings from an adult cat implanted chronically with a microelectrode array in the L7 dorsal root ganglia (DRG). The methods for implanting electrodes and recording in the DRG have been described in detail in (Weber et al. 2007). A summary of these methods follows. All procedures were approved by the University of Alberta Animal Care and Use Committee. All surgical procedures were conducted with the use of isoflurane anesthesia. A laminectomy was performed to expose the DRG on one side of the lower lumbar spine. A single Utah Electrode Array (UEA, Blackrock Microsystems, Inc.) comprising 36 electrodes arranged in a 9×4 configuration was implanted in the L7 DRG. The lead wires were anchored to the L5 spinous process and terminated in a percutaneous connector attached to an implanted stainless steel saddle affixed to the iliac crests.

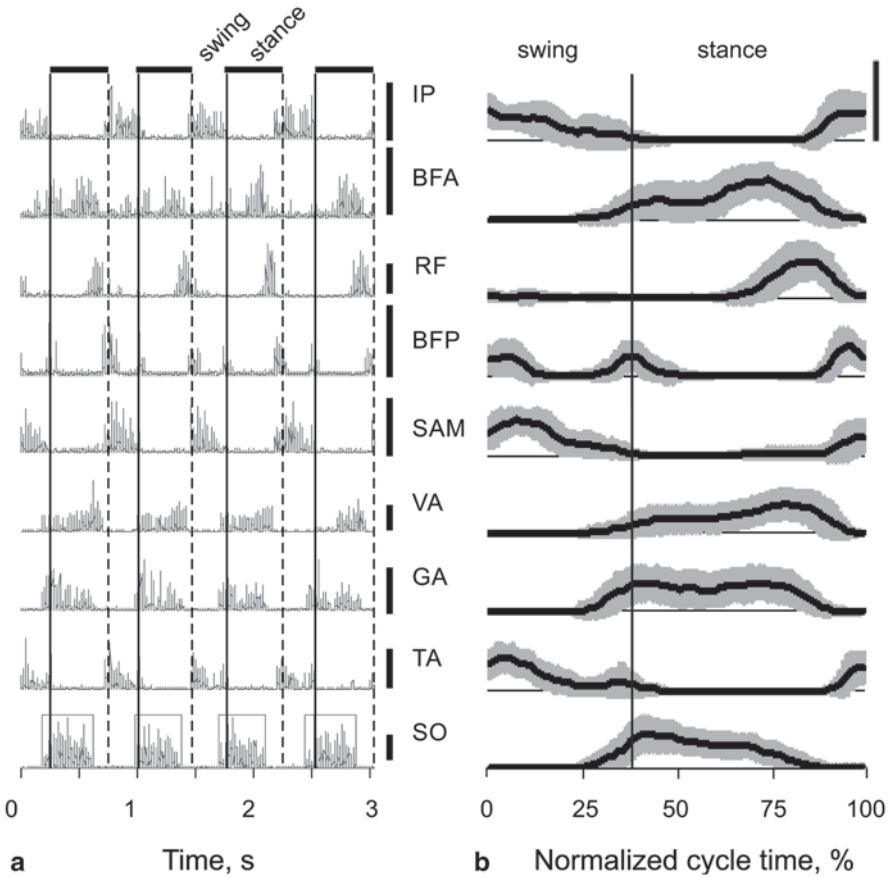


Fig. 10.2 EMG activity of 9 cat hindlimb muscles during walking. Muscle abbreviations are the same as in Fig. 10.1c. **a** Example of rectified EMG signals recorded during 4 cycles of walking in one representative cat. Horizontal bars on the top and corresponding vertical dashed lines indicate stance phases identified using force plates or kinematics. Vertical bars on the right indicate scale of 0.5 mV. The dashed-line rectangles in the bottom plot (SO) demonstrate an example of identified EMG bursts; the activity between the bursts was set to zero before low-pass filtering was applied to the rectified signal. **b** Normalized mean \pm SD rectified and low-pass filtered EMG patterns of multiple walking cycles and cats (total number of cycles analyzed for each muscle were between 84 and 169; data for SAM were obtained from 2 cats, for IP from 3 cats, for BFP from 4 cats, and for BFA, RF, VA, GA, TA, and SO from 5 cats). The vertical line separates the swing and stance phase. The vertical bar on top right corresponds to the maximal muscle recruitment magnitude. During walking, peak EMG activities for each muscle were set to be a certain proportion of the maximum: IP=0.2, BFA=0.5, RF=0.5, BFP=0.2, SAM=0.5, VA=0.3, GA=0.215, TA=0.2, and SO=0.9; adopted and modified from (He et al. 1991)

Neural recordings and hindlimb kinematics were recorded as the cat walked on a treadmill at an average speed of 0.4 m/s. Hindlimb kinematics were recorded using a high-speed video camera and reflective markers stuck to the skin over the iliac

crest and centers of the hip, knee, ankle, and metatarsophalangeal (MTP) joints. Heel-strike and toe liftoff times were identified manually in the video records and marked for segmentation of individual step cycles. During recording sessions, a 100-channel pre-amplifier was connected to the UEA connector and the amplified signals were sampled at 30,000 samples/s. Thresholds for spike detection were set for each channel and a 1–1.6 ms segment of the spike was recorded each time the signal exceeded the threshold. Spike-sorting for each electrode was performed off-line using custom Matlab (Mathworks, Inc) software as described in (Shoham et al. 2003). The sorted spike event times were used to calculate a time series of instantaneous firing rates for each sensory neuron (see below).

A series of tests were performed before or after the treadmill experiments to identify each receptor type. During the unit identification tests, the cat was anesthetized with isoflurane gas to permit a thorough examination of the limb. The identification process began with the localization of the receptive field of each receptor, identified by palpating the leg. Then, its response to (1) joint motion, (2) pressure, (3) blowing and (4) vibration was studied. Units that responded to blowing and very light brushing of the fur were identified as hair receptors (located in the skin at the base of the hair follicle). Units that responded reliably to light pressure or localized skin stretch were also classified as cutaneous afferents.

For the purpose of this study, activity of four paw pad cutaneous afferents continuously recorded in 11 walking cycles were selected for further analysis. Instantaneous firing rates of each cell were computed at 25 ms intervals (Weber et al. 2007) and then interpolated for each percent of a walking cycle using a cubic spline function. The ensemble activity of paw pad cutaneous afferents was obtained by averaging the interpolated firing rates for each percent of the cycle across all recorded cycles and four cells (Fig. 10.7d, thin line). To compare the mean afferent activity with the mean vertical ground reaction force recorded separately in five different animals as described above, the mean duty factor (stance time/cycle time) of the cycles collected for afferent activity was made equal to the mean duty factor obtained in locomotor mechanics experiments. Subsequently, the mean afferent activity was normalized to the new stance and swing durations separately.

10.2.2 Musculoskeletal Model

10.2.2.1 Limb Dynamics

The cat hindlimbs with the pelvis and trunk were modeled as a 10 degrees-of-freedom sagittal plane system of rigid segments interconnected by frictionless revolute joints (Fig. 10.1a, b). Interactions of the hindlimbs with the ground and the trunk with the fore-legs, neck and head were modeled by linear springs and dampers (Fig. 10.1a and Table 10.1; e.g., (van den Bogert et al. 1989)). The ground reaction viscoelastic forces were computed as a function of velocity and displacement of the leg endpoint during stance:

Table 10.1 Parameters of the limb model

Parameters	Segments				
	Trunk	Pelvis	Thigh	Shank	Foot ^a
Center of mass location ^b , mm	122.5	27.5	43.1	43.4	33.5
Mass, g	1448.8	324.6	149.5	63.5	21.7
Moment of inertia, g · mm ²	7249930	81524	140063	59201	9147
Length, mm	245.0	54.9	97.3	102.5	68.9
Parameters of linear springs and dampers at model contact sites					
	Foot-ground	Joints		Distal trunk	
Coefficient of stiffness	1.25 N/mm	3000 N/rad		6 N/mm	
Coefficient of viscosity	28.5 N · ms/mm	18000 N · ms/rad		35 N · ms/mm	

Body segment parameters were calculated from body mass and segment length using the regression equations from (Hoy and Zernicke 1985)

^a Foot included tarsals and digits

^b Distance from the proximal joint

$$\begin{aligned} F_{Gx} &= -k_g \Delta x - b_g \dot{x} \\ F_{Gy} &= -k_g \Delta y - b_g \dot{y}, \end{aligned} \quad (10.1)$$

where F_{Gx} and F_{Gy} are the horizontal and vertical components of the ground reaction force vector, constants k_g and b_g ($b_g = 0$ for $\dot{y} > 0$) are stiffness and viscosity coefficients (Table 10.1) found using optimization (see below); Δx and Δy are foot endpoint displacements during the stance phase from the initial point of contact at the ground level; dots indicate time derivatives. Similarly, the viscoelastic force applied at the distal trunk was a function of the trunk's tip deviation from preset horizontal and vertical positions and velocities. Mass, moment of inertia, and the location of the center of mass of each body segment (Table 10.1) were calculated based on animal mass and measured segment lengths using the regression equations from (Hoy and Zernicke 1985).

The dynamic equations of system motion can be written in a vector form:

$$\ddot{\mathbf{q}} = \mathbf{I}^{-1}(\mathbf{q}) [\mathbf{C}(\mathbf{q}, \dot{\mathbf{q}}) + \mathbf{G}(\mathbf{q}, \dot{\mathbf{q}}) + \mathbf{S}(\mathbf{q}, \dot{\mathbf{q}}) + \mathbf{M}(\mathbf{q}, \dot{\mathbf{q}}, \mathbf{t})] \quad (10.2)$$

where \mathbf{q} , $\dot{\mathbf{q}}$ and $\ddot{\mathbf{q}}$ are vectors of the generalized displacements, velocities and accelerations, \mathbf{I} is the system inertia matrix, \mathbf{C} is the vector of Coriolis and centrifugal forces, \mathbf{G} is the vector of external generalized forces, \mathbf{S} is the vector of viscoelastic generalized forces at the joints (passive joint moments) and \mathbf{M} is the vector of muscle generalized forces (muscle moments). Viscoelastic passive moments at the joints were engaged only if computed joint angles exceed the nominal locomotor range of joint motion: 127° (fixed angle), 50°–180°, 45°–160°, and 45°–160° for pelvis-trunk articulation, hip, knee and ankle, respectively. These generalized passive forces at j -th joint were computed as $S_j = -k_p \Delta q_j - b_p \dot{q}_j$, where Δq_j is the deviation of joint angle from the nominal range, \dot{q}_j is angular velocity, and k_p and b_p coefficients of stiffness and viscosity given in Table 10.1.

10.2.2.2 Muscle Dynamics

The hindlimb model was driven by 18 Hill-type muscle actuators (9 per hindlimb) that represented major hindlimb muscles (Fig. 10.1c). The location of each muscle-tendon unit (MTU) with respect to the joints was described geometrically using the measured origin and insertion points of the muscle and pulleys representing bone protuberances over which the muscle wraps (Table 10.2). MTU lengths and moment arms were computed using muscle and joint parameters from Table 10.2 as functions of joint angles.

Equations of Muscle Dynamics and Properties of Tendon and Muscle The contraction dynamics of the MTU were described by a Hill-type model (Fig. 10.1d, e.g., (Zajac 1989; He et al. 1991; Brown et al. 1996b; Sandercock and Heckman 1997) taking into account muscle mass, angle of pennation, the force-length-velocity relations of the contractile element and the force-length relation of the serial (tendon) and parallel elastic elements. Muscle contractile dynamics were described by the following differential equation:

$$\dot{V}_T = [F_T - F_M \cos \alpha] / m, \quad (10.3)$$

where

$$F_T = F_T^{Max} [F_{TN}(L_T) + b_T V_T]; \quad (10.4)$$

$$F_M = F_M^{Max} [F_{CE}(L_M) F_{CE}(V_M) k_u^{\max} A + F_{PEN}(L_M) + b_M V_M]; \quad (10.5)$$

F_T , L_T , and V_T are tendon force, length and velocity; F_M , L_M , and V_M are muscle fiber force, length and velocity; α is the pennation angle; b_T and b_M are coefficients of viscosity for the tendon and muscle; m is muscle mass; $F_{TN}(L_T)$, $F_{PEN}(L_M)$ and $F_{CE}(L_M)$ are the normalized force-length relations for the tendon, muscle parallel elastic element, and the muscle contractile element (see equations for these relationships below and in Table 10.3); $F_{CE}(V_M)$ is the normalized force-velocity relation for the muscle contractile element (see below and Table 10.3); F_T^{Max} and F_M^{Max} are the maximal isometric tendon and muscle force at optimum length of the contractile element and $F_T^{Max} = F_M^{Max} \cos(\alpha_0)$ (α_0 is pennation angle at the optimal contractile element length); k_u^{\max} is muscle maximal activation during walking ($0 \leq k_u^{\max} \leq 1$, modified from (He et al. 1991), see Table 10.2); and A is time dependent muscle activation obtained from the first-order differential equation describing the muscle excitation (EMG)-activation (active state) dynamics (Zajac 1989; He et al. 1991):

$$\frac{dA(t)}{dt} + \left\{ \frac{\tau_{act}}{\tau_{deact}} + \left[1 - \frac{\tau_{act}}{\tau_{deact}} \right] u(t) \right\} \frac{A(t)}{\tau_{act}} = \frac{u(t)}{\tau_{act}} \quad (10.6)$$

Table 10.2 Geometric and physiological parameters of hindlimb muscles

Parameter	Muscle	IP	BFA	RF	BFP	SAM	VA	GA	TA	SO
m , g		17.6	28	9.5	41.3	8.5	27.5	24.8	5.5	3.5
F_M^{\max} , N		64.3	82.9	77.3	147.5	35.2	435	54.8	36.2	36.4
α , deg		0	14.0	7.0	7.0	0.0	13.7	19.0	7.0	7.0
L_{IP} , mm		15.5	17.5	80.0	14.0	17.5	35.5	80.8	25.0	20.9
L_{IP}/L_0		0.5	0.5	4.0	0.1	0.1	2.0	6.0	1.0	1.0
L_{PEff}/L_0		1.0	0.9	1.0	1.0	0.7	0.9	0.85	1.0	0.9
R_1 , mm		5.0	5.0	5.0	5.0	5.0	7.1	5.0	5.0	5.0
R_2 , mm		-	-	7.1	5.0	5.0	-	5.0	-	-
a_1 , mm		36.8	8.0	14.6	8.0	32.0	55.1	5.0	6.2	36.1
a_2 , mm		5.0	40.8	7.1	24.9	20.1	7.1	15.0	7.3	15.0
ϕ_1 , deg		0	141	0	141	0	0	0	0	0
ϕ_2 , deg		0	0	145	0	0	145	-174	0	-174
k_M^{\max}		0.2	0.6	0.59	0.22	0.6	0.28	0.17	0.24	1
R_{I_0} , imp/s		12	16	34	18	31	58	70	128	62
R_{II_0} , imp/s		32	62	16	16	36	85	108	166	33

IP iliopsoas, *BFA* biceps femoris anterior, *RF* rectus femoris, *BFP* biceps femoris posterior, *SAM* sartorius medial, *VA* vastus, *GA* gastrocnemius, *TA* tibialis anterior, *SO* soleus. m , muscle mass; F_M^{\max} , maximal isometric muscle force at optimal fiber length L_M^0 ; α , pennation angle at L_M^0 , estimated from (Sacks and Roy 1982); L_{IP} , tendon rest (slack) length; L_{IP}/L_{MIP} , tendon rest length-fiber optimal length ratio, estimated from (Sacks and Roy 1982; Zajac 1989; Prilutsky et al. 1996); L_{PEff}/L_{MIP} , resting (slack) length of the parallel elastic element normalized to optimal fiber length (estimated from (Gareis et al. 1992; Brown et al. 1996a)); R_1 , joint radius; R_2 , radius of the other (distal joint) crossed by a two-joint muscle; a_1 , muscle-tendon unit (MTU) origin-to-joint center distance; a_2 , MTU attachment-to-joint center distance; ϕ_1 , angle between segment axis and position vector from joint center to muscle origin, ϕ_2 , angle between segment axis and position vector from joint center to muscle attachment; k_M^{\max} , peak of normalized activation during walking, obtained using estimates from (He et al. 1991); R_{I_0} and R_{II_0} , mean firing frequencies of Ia and II afferents, respectively, set based on experimental recordings (see Fig. 10.7). Initial values for muscle mass m and maximal force F_M^{\max} before optimization were calculated as $m = PCSA \cdot L_M^0 \cdot \rho_m$ and $F_M^{\max} = \sigma \cdot PCSA$, respectively, where $PCSA$ and L_M^0 are the muscle physiological cross-sectional area and fiber length taken from (Sacks and Roy 1982), ρ_m and σ are muscle density (1.0564 g/cm³) and maximum muscle stress (2.25 N/cm²) (Spector et al. 1980). MTU length was calculated as the length of straight line from muscle origin to attachment except when this line touched a joint pulley in which case the part of muscle length was calculated assuming that the muscle wraps around the joint surface represented by a pulley with a given diameter

Table 10.3 Parameters of tendon and muscle model

Parameter	Equation
Tendon $F_T(L_T)$ relation	
k_{T1}	0.1
k_{T2}	90
Parallel element $F_{PE}(L_{PE})$ relation	
k_{PE1}	0.0075
k_{PE2}	11.6
Muscle $F_{CE}(V_M)$ relation	
Muscle	a_V V_{max} (m/s)
IP	3.70 0.578
BFA	9.50 0.643
VA	2.40 0.266
TA	5.90 0.813
SO	1.10 0.176
RF	5.00 0.288
BFP	9.50 0.624
SAM	3.70 1.491
GA	2.28 0.259
Muscle $F_{CE}(L_M)$ relation	
ω	0.55
ρ for $L_{-ITD}/L_0 \leq 1$	6
ρ for $L_{-ITD}/L_0 > 1$	3
β	1.55
Muscle and tendon viscosity coefficients	
b_T (N·s/m)	0.02
b_M (N·s/m)	0.02

$$F_T(L_T) = \frac{k_{T1}}{k_{T2}} \left\{ \exp(k_{T2} [L_T / L_{T0} - 1]) - 1 \right\}$$

$$F_{PE}(L_M) = \frac{k_{PE1}}{k_{PE2}} \left\{ \exp(k_{PE2} [L_M / L_0 - 1]) - 1 \right\}$$

$$F_{CE}(V_M) = \begin{cases} b_0 + b_1 V_M & (V > 0) \\ b_0 + V_M & \\ \frac{V_M^{\max} + V_M}{V_M^{\max} - a_V V_M} & (V < 0) \end{cases}$$

$$b_0 = V_M^{\max} \frac{0.8}{a_V + 1},$$

$$b_1 = \frac{1.8(V_M^{\max} + b_0) - b_0}{V_M^{\max}}$$

$$F_{CE}(L_M) = \exp \left(- \left[\frac{(L_M / L_0)^\beta - 1}{\omega} \right]^\rho \right)$$

See Eq. (10.4)

See Eq. (10.5)

Table 10.3 (continued)

Parameter	Equation	
Muscle activation dynamics parameters		
Muscle	τ_{act} , ms	τ_{act}/τ_{deact}
IP	10.0	0.8
BFA	10.0	0.5
VA	20.2	0.5
TA	24.6	0.5
SO	42.6	0.6
RF	10.0	0.5
BFP	24.8	0.6
SAM	10.0	0.5
GA	20.7	1.0

L_T is tendon length; L_M and V_M are muscle fiber length and velocity; V_{max} is muscle maximum shortening velocity (taken from (Spector et al. 1980) for SO and GA and estimated for the other muscles based on the assumption that V_{max} is proportional to the expression $L_{Mo} \cdot (1 - S / 100)$, where L_{Mo} is optimal muscle fiber length (Sacks and Roy 1982) and S is the percentage of slow-twitch fibers (Ariano et al. 1973); a_V is coefficient in the equation for $F_{CE}(V_M)$, it was calculated from equation $a_V = 0.00915 \cdot S - 0.00467$, $r = 0.974$; (Baratta et al. 1995), where S is the percentage of slow-twitch fibers; b_T and b_M are coefficients of viscosity for tendon and muscle contractile element, respectively; $F_{CE}(L_M)$ and $F_{CE}(V_M)$ are normalized force-length and force-velocity relationships for contractile element; $F_T(L_T)$ and $F_{PE}(L_M)$ are tendon and parallel element force-length relations; τ_{act} and τ_{deact} are muscle activation and deactivation time constants; A is muscle activation (see Eq. 10.6). Coefficient ρ was set to 6 for muscles with short tendon ($L_{T0}/L_0 \leq 1$): IP, BFA, BFP, SAM, TA, SO; ρ was set to 3 for muscles with long tendon ($L_{T0}/L_0 > 1$): RF, VA, GA (see text for further explanations)

where $u(t)$ is rectified, low-pass filtered and normalized to its peak EMG activity ($0 \leq u(t) \leq 1$, see Fig. 10.2b); τ_{act} and τ_{deact} are the activation and deactivation time constants. Definitions, values, and sources for the above muscle-tendon-activation parameters and relations are given in Tables 10.2 and 10.3.

Tendon Force-Length Relation Two general forms of the normalized force-length relation for the tendon were examined (see Eq. 10.7 and Table 10.3). The first form of the normalized relation $F_{TN}(L_T)$ (see Eq. 10.4) was adopted from (Siebert et al. 2008) and slightly modified (see Fig. 10.3a):

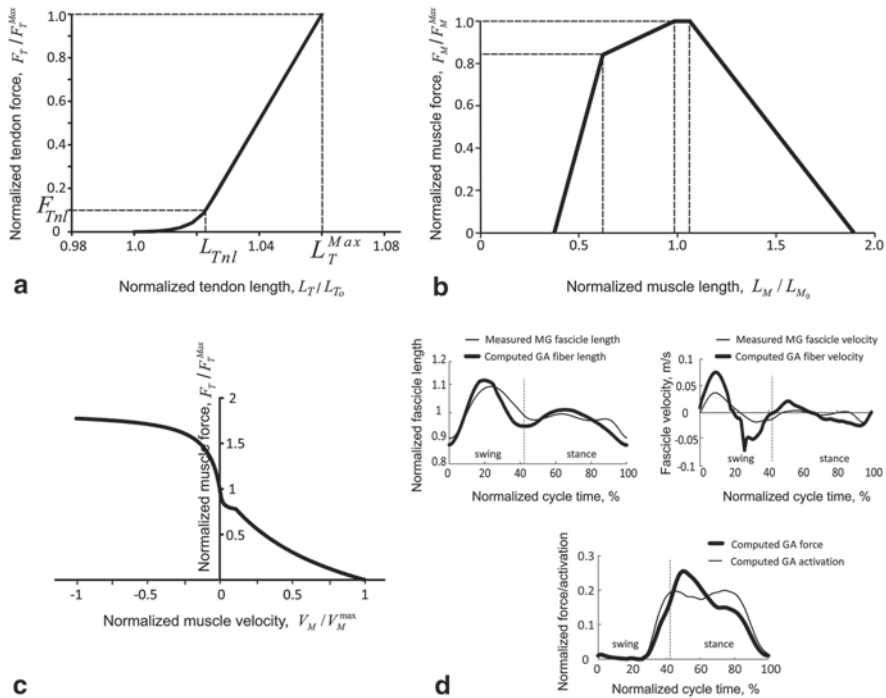


Fig. 10.3 Modeling the tendon force-length and contractile element force-length and force-velocity properties. **a** Normalized tendon force-length relation adopted from (Siebert et al. 2008). Parameters of the relation (see Eq. 10.7) were found by minimizing the difference between simulated and measured muscle fascicle length during the cycle of cat walking (see text and panel **d**). **b** Normalized force-length relation for the contractile element adopted from (Gordon et al. 1966) and (Siebert et al. 2008) (see text). **c** Normalized force-velocity relation for the contractile element adopted from (Edman 1988) (see Eq. 10.8 and the corresponding text). **d** Fascicle length and velocity during the walking cycle (*top* panels) computed for gastrocnemius (GA) after minimizing cost function Z_1 (Eq. 10.10) and measured in medial gastrocnemius (MG) in (Maas et al. 2009). *Bottom* panel shows computed MG force and activation after minimizing cost function Z_1 (see text)

$$F_T = \begin{cases} F_T^{Max} \cdot F_{Tnl} \frac{\exp\{k_{Tnl} \cdot [(L_T / L_{To}) / L_{Tnl}]\} - 1}{\exp(k_{Tnl}) - 1}, & 1 < L_T / L_{To} < L_{Tnl} \\ F_T^{Max} \cdot [F_{nl} + k_{Tl} \cdot (L_T / L_{To} - L_{Tnl})], & L_T / L_{To} \geq L_{Tnl} \end{cases}, \quad (10.7)$$

where F_T and L_T are tendon force and length, L_{To} is the tendon rest (slack) length in mm, L_{Tnl} and F_{Tnl} are the tendon length normalized to L_{To} and force corresponding to the point of separation between the nonlinear and linear parts of the tendon force-length relation, k_{Tnl} and k_{Tl} are the stiffness constants for the nonlinear and linear parts of the relation, L_T^{Max} is the tendon length corresponding to F_T^{Max} (see Eq. 10.4).

The second form of the relation $F_{TN}(L_T)$ and its parameters are presented in Table 10.3. This form was used in computations of afferent feedback signals (see below).

Isometric Force-Length Relation for the Contractile Element Again, two general forms of the normalized isometric force-length relation $F_{CE}(L_M)$ were examined (see Fig. 10.3b and Table 10.3). The first form (Fig. 10.3b) was derived from the normalized force-length relation of the frog sarcomere (Gordon et al. 1966) and adapted to the cat muscle (Siebert et al. 2008). The relation is described by 4 straight lines connecting the following points in the $L_M / L_{M_0} - F_M / F_M^{Max}$ plane: (0.39, 0), (0.64, 0.84), (1, 1), (1.08, 1) and (1.9, 0). The second form of the relation was adopted from (Markin et al. 2010); the equation and its parameters are included in (Table 10.3).

Force-Velocity Relation for the Contractile Element Initially we adopted the force-velocity relation of the contractile element, $F_{CE}(V_M)$, in the double-hyperbolic form proposed by (Edman 1988) (Fig. 10.3c):

$$F_{CE} = \begin{cases} \frac{V_M^{max} + V_M}{V_M^{max} - aV_M}, & V_M > V_{Mtr} \\ k_{FV} + \frac{g}{V_M - h}, & V_{Mtr} > V \end{cases}, \quad (10.8)$$

where V_{Mtr} corresponds to velocity at which the Hill force-velocity equation (Hill 1938) starts to deviate from the Edman's equation. Parameters k_{FV} , g , and h describe the hyperbolic equation in the velocity range $0 < V_M < V_{Mtr}$ and were derived based on the following three conditions:

1. The derivative of the normalized force over the normalized velocity at $V_M / V_M^{max} = 0$ is $k_d = 100$ (based on Fig. 2c in Edman 1988).
2. $F_{CE}^{max} = 1$ at $V_M = 0$.
3. Normalized muscle force at the transition from the Hill equation to Edman equation (at velocity $V_M = V_{Mtr} = 0.11V_M^{max}$) is $F_{CE} = 0.78$ (Edman 1988).

Condition 1 leads to

$$g = -k_d h^2, \tag{10.9a}$$

Condition 2 combined with Eq. (10.9a) gives

$$k_{FV} = F_M^{\max} - k_d h, \tag{10.9b}$$

and condition 3 combined with Eqs. (10.9a) and (10.9b) gives

$$h = \frac{V_{Mtr} (F_{CE}^{\max} - F_{CEtr})}{V_{Mtr} \cdot k_d - (F_{CE}^{\max} - F_{CEtr})}. \tag{10.9c}$$

Parameters k_{FV} , g , and h for the hyperbolic equation at muscle stretch velocities $V_M < 0$ were derived from the following conditions:

- 1a. The derivative of the normalized force over the normalized velocity at $V_M / V_M^{\max} = 0$ is $k_d = 50$ (based on Fig. 7 in Edman 1988).
- 2a. $F_{CE}^{\max} = 1$ at $V_M = 0$.
- 3a. F_{CE} approaches an asymptote $k_{FV} = 1.85$ at muscle elongation velocity V_M approaching minus infinity.

From condition 1a follows Eq. (10.9a); condition 2a and Eq. (10.9a) leads to

$$h = \frac{F_{CE}^{\max} - k_{FV}}{k_d} \tag{10.9d}$$

Thus the parameters for the force-velocity relation are (see Fig. 10.3c):

$$k_{FV} = \begin{cases} F_{CE}^{\max} - k_d h, & 0 < V_M / V_M^{\max} < V_{Mtr} \\ 1.85, & V_M / V_M^{\max} < 0 \end{cases},$$

$$h = \begin{cases} \frac{V_{Mtr} (F_{CE}^{\max} - F_{CEtr})}{V_{Mtr} \cdot k_d - (F_{CE}^{\max} - F_{CEtr})}, & 0 < V_M / V_M^{\max} < V_{Mtr} \\ \frac{F_{CE}^{\max} - k_{FV}}{k_d}, & V_M / V_M^{\max} < 0 \end{cases},$$

$$k_d = \begin{cases} 100, & 0 < V_M / V_M^{\max} < V_{Mtr} \\ 50, & V_M / V_M^{\max} < 0 \end{cases}.$$

The other form of the force-velocity relation and its parameters are in Table 10.3 (see below).

10.2.2.3 Tuning Muscle Model Parameters and Validation of Muscle-Tendon Model

Since the output of muscle models (typically muscle force) is sensitive to errors in model parameters (Brown et al. 1996b; Scovil and Ronsky 2006; De Groot et al. 2010), it is important to accurately measure the parameters that have the greatest effect on the model performance (typically tendon properties as well as muscle maximum force) when possible or tune them so that the computed muscle force and simulated locomotor mechanics match the experimental data as close as possible. In this study, parameters of the equations of muscle dynamics (Eqs. 10.3–10.8) were optimized within the physiological ranges in several stages.

Stage 1: Tuning Tendon Model Parameters In stage 1, parameters of the tendon L_{T_0} , k_{TI} , L_{Tnl} and L_T^{\max} (see Eq. 10.7) and optimal muscle fiber (contractile element) length L_{M_0} were tuned by minimizing the difference (Eq. 10.10) between computed and measured during cat level walking muscle fascicle length and velocity separately for muscle-tendon actuators with a relatively long tendon, e.g., medial gastrocnemius (MG, $L_{T_0} / L_{M_0} > 1$, where L_{T_0} and L_{M_0} are the tendon rest and muscle fiber optimum length, respectively) and a short tendon, e.g., soleus (SO, $L_{T_0} / L_{M_0} \leq 1$). Inputs for these calculations were EMG activity of these muscles and hindlimb joint angles recorded during walking in 5 cats as described above. It was assumed that other hindlimb muscles with relatively long and short tendons had the same normalized tendon properties as those of MG and SO, respectively. The muscle actuators with relatively long tendons included gastrocnemius (GA), vastii (VA) and rectus femoris (RF); the actuators with relatively short tendons consisted of soleus (SO), tibialis anterior (TA), sartorius medial (SAM), biceps femoris posterior (BFP), biceps femoris anterior (BFA) and iliopsoas (IP). This muscle classification was based on values of L_{T_0} and L_{M_0} reported by (Sacks and Roy 1982; Zajac 1989; Prilutsky et al. 1996). Tendon model parameters L_{T_0} , k_{TI} , L_{Tnl} and L_T^{\max} and optimal muscle fiber length L_{M_0} for MG and SO were found using a numerical minimization of the cost function Z_1 for each muscle separately:

$$Z_1 = \frac{\sum_{i=1}^N (L_{M_i} - L_{M_i}^e)^2}{R_{L_M}^2} + \frac{\sum_{i=1}^N (V_{M_i} - V_{M_i}^e)^2}{R_{V_M}^2} + \frac{\sum_{i=1}^N (F_{M_i} - A_i)^2}{A_0^2}, \quad (10.10)$$

where L_{M_t} and $L_{M_t}^e$ are computed and measured during cat walking mean muscle fascicle length at the time instant t ($t=1,2,\dots,N$), respectively; R_{M_t} is the range of measured muscle fascicle length changes in the walking cycle; V_{M_t} and $V_{M_t}^e$ are computed and measured muscle fascicle velocity, respectively; $R_{V_{M_t}}$ is the range of measured muscle fascicle velocity changes in the walking cycle; F_{M_t} is computed muscle force; A_t is muscle activation computed from recorded muscle activity (low-pass filtered EMG, Fig. 10.2b) using Eq. (10.6) in which muscle activation and deactivation constants τ_{act} and τ_{deact} were assumed to be 25 and 50 ms, respectively, for all muscles for the purpose of this optimization. The third term in Eq. (10.10) was introduced to ensure that in the optimal solution the muscle does not produce noticeable passive force when the muscle is not activated.

The fascicle length and fascicle velocity of SO and MG muscles during the walking cycle were measured in 4 cats in a previous study (Maas et al. 2009) and averaged across walking cycles and cats (Fig. 10.3d, thin lines). Muscle-tendon unit (MTU) length trajectories of SO and MG were computed from recorded joint angles using a hindlimb geometric model.

Dynamic optimization problem of minimizing cost function Z_1 (Eq. 10.10) was solved under the constraints described by equations of muscle dynamics (10.3–10.6) and Eq. (10.11):

$$L_{M_1} = L_{M_1}^e; \quad V_{M_1} = V_{M_1}^e; \quad L_{M_t} \cdot \cos \alpha + L_{T_t} = L_{MTU_t} \quad (t = 1, 2, \dots, N), \quad (10.11)$$

where L_{M_1} and $L_{M_1}^e$ are initial values of computed and experimental muscle fascicle length; V_{M_1} and $V_{M_1}^e$ are initial values of computed and experimental muscle fascicle velocity; L_{MTU_t} is MTU length at time instant t computed from recorded joint angles and the geometric model of SO and MG. Additional inequality constraints kept the optimized model parameters within the physiological ranges reported in the literature (Spector et al. 1980; Sacks and Roy 1982; Siebert et al. 2008).

The optimization problem was solved using a parallel simulated annealing algorithm (Corana et al. 1987) and Open Multi-Processing Interface for SO and GA separately. The equations of muscle dynamics (Eqs. 10.3–10.8) were integrated numerically using a custom C++ program on a PC with Intel Xeon Quad Core processors. The equations were integrated over a complete walking cycle by a second order Runge-Kutta method with a constant 0.075-ms time step.

The found optimal tendon model parameters provided the minimal possible difference between computed and measured muscle fascicle length and velocity for both SO and MG muscles. An example of this comparison for MG during a cycle of walking is shown in Fig. 10.3d, along with the comparison between computed MG force and activation. The tuned tendon model parameters for SO and MG were used in the subsequent calculations for the muscles with relatively short and long tendons, respectively. The optimal parameters for SO were $L_{M_0} = 42.00$ mm, $L_{T_0} = 56.03$ mm, $k_{Tnl} = 4.70$, $L_{Tnl} = 0.024$, $L_T^{Max} = 0.060$; for MG they were $L_{M_0} = 27.00$ mm, $L_{T_0} = 75.30$ mm, $k_{Tnl} = 8.00$, $L_{Tnl} = 0.01$, $L_T^{Max} = 0.120$.

To validate the muscle model and its parameters, we compared simulated force time-histories of fully activated SO during imposed isovelocity stretch and shortening computed using Eqs. (10.3–10.8) with experimental recordings from a cat SO muscle obtained in (Sandercock and Heckman 1997). In those experiments, cat SO was fully activated by 60-Hz tetanic stimulation trains and when the muscle reached its maximum isometric force, MTU length isovelocity ramps were imposed by a muscle puller; shortening and lengthening speeds ranged between -0.2 m/s and 0.08 m/s (Fig. 10.4). For the simulations, the optimum fascicle length and maximum

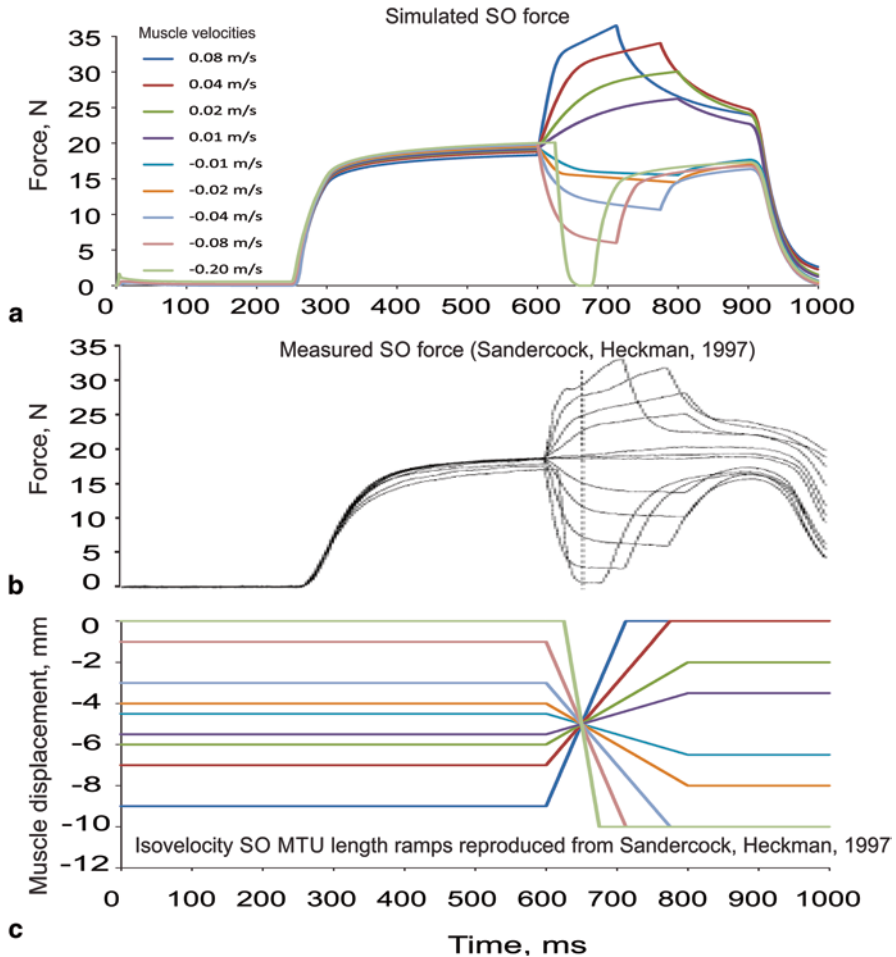


Fig. 10.4 Simulated **a** and experimental **b** force traces of fully activated cat soleus (SO) in response to isovelocity changes in muscle-tendon unit length **c**. Experimental force traces were adopted with permission from Fig. 2 of (Sandercock and Heckman 1997), American Physiological Society. Parameters of SO tendon and muscle contractile element used in these simulations were: $F_M^{\max} = 20.8$ N, $L_{M_0} = 42.00$ mm, $L_{T_0} = 56.03$ mm, $k_{Tnl} = 4.70$, $L_{Tnl} = 0.024$, $L_T^{Max} = 0.060$ (see Eq. 10.7)

SO force at the optimum muscle length were selected to match values reported in (Sandercock and Heckman 1997). Simulated SO forces were in good agreement with the measured ones in terms of peak values and patterns.

Stage 2: Tuning Muscle Model Parameters In stage 2 of tuning model parameters, the found optimal tendon parameters were fixed and muscle specific parameters F_M^{Max} , τ_{act} and τ_{deact} (see Eqs. 10.4–10.6), and distances of muscle origin and attachments from the joint centers a_1 and a_2 were tuned for each muscle. The values of these muscle parameters were found by minimizing the difference between computed and experimental resultant muscle moments at hindlimb joints and between computed normalized muscle force and computed normalized activation (cost function Z_2 , Eq. 10.12) using as input to computations the recorded EMG activity of each muscle (Fig. 10.2b) and experimental angles at the ankle, knee and hip joints (Fig. 10.5a):

$$Z_2 = \frac{w_M}{3N} \sum_{j=1}^3 \sum_{t=1}^N \left[\left(M_{jt} - M_{jt}^e \right) / SD_j^M \right]^2 + \frac{w_F}{9N} \sum_{i=1}^9 \sum_{t=1}^N \left[\left(F_{Mit} - A_{it} \right) / SD_i^u \right]^2, \quad (10.12)$$

where M_{jt} and M_{jt}^e are computed and experimental joint moments at the j -th joint of the right hindlimb at the t -th time frame; F_{Mit} is computed force of the i -th muscle; A_{it} is muscle activation obtained from recorded EMG (see Eq. 10.6) of the i -th muscle; SD_j^M and SD_i^u are standard deviations of the j -th joint moment and the i -th muscle normalized EMG averaged over a walking cycle; N is number of time frames; $w_M = 5$ and $w_F = 1$; subscripts j and i designate 3 joints and 9 muscles of the right hindlimb, respectively. Equations of muscle dynamics (10.3–10.8) and MTU length and velocity of each muscle during walking cycle (computed from recorded joint angles) were used as constraints for the optimization problem. In addition, the optimal solution was constrained by the physiological range of values reported in the literature for the parameters F_M^{Max} , τ_{act} and τ_{deact} (Sacks and Roy 1982; Zajac 1989; He et al. 1991; Gareis et al. 1992; Baratta et al. 1995; Scott and Loeb 1995; Brown et al. 1996a, b). Minimization of cost function Z_2 gave a close match between the computed and experimental resultant joint moment (Fig. 10.5c, blue dotted lines).

Stage 3: Tuning Parameters of Viscoelastic Interactions with the External Environment In stage 3, the found optimal parameters of the tendon and muscle models were fixed (except constants τ_{act} and τ_{deact}) and parameters of viscoelastic interactions of the hindlimb model with the external environment (coefficients of stiffness and viscosity, Table 10.1), constant forward velocity of the trunk distal endpoint (Fig. 10.1a), and activation and deactivation constants τ_{act} and τ_{deact} were tuned by minimizing the differences between simulated and recorded joint angles, ground reaction forces and joint moments. The constants τ_{act} and τ_{deact} obtained in stage 2 optimization were re-optimized for each muscle to ensure the best possible match between simulated and experimental walking mechanics.

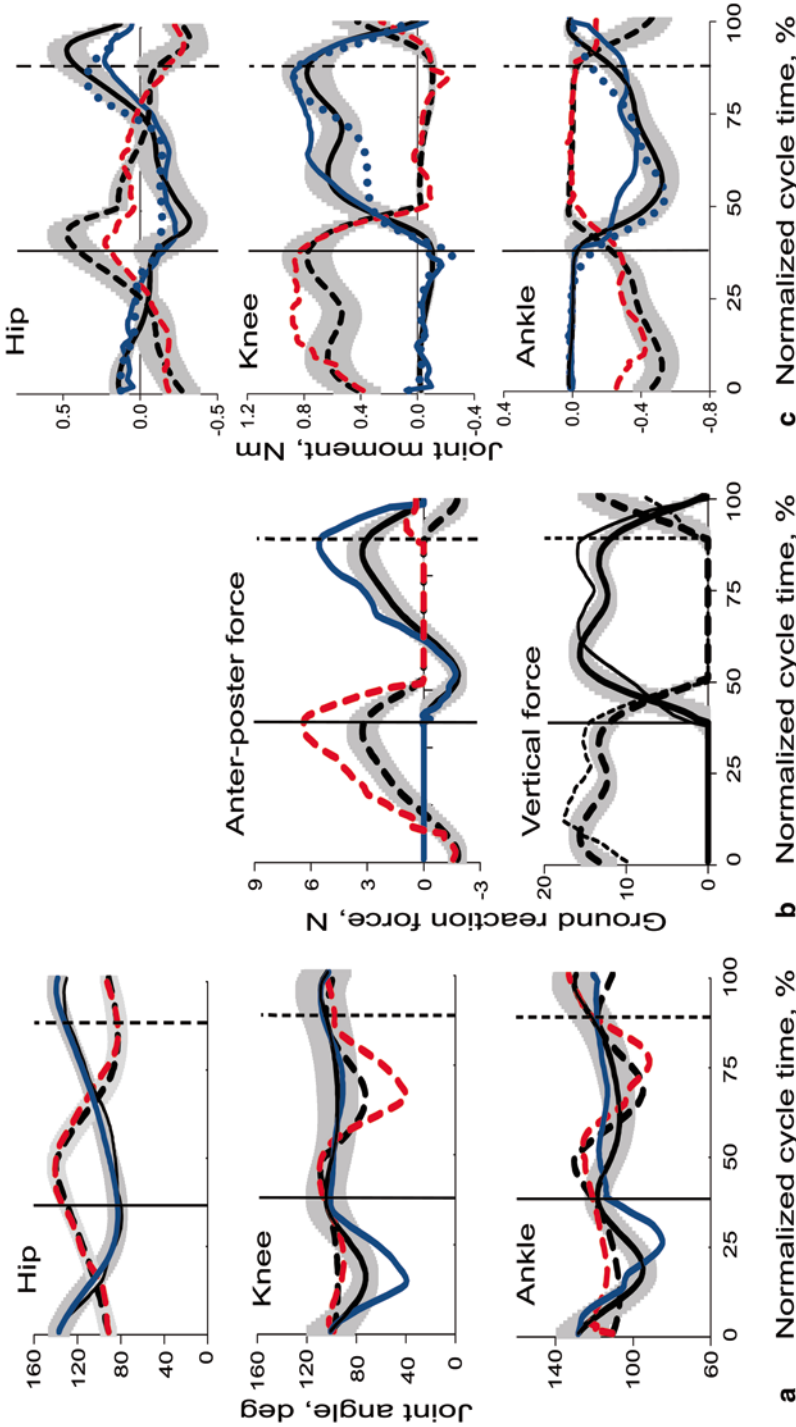


Fig. 10.5 Recorded mean (black lines) \pm SD (gray shadow) and computed (blue and red lines) joint angles **a**, ground reaction forces **b** and joint moments **c** for two hindlimbs during a cycle of walking. Simulations were based on the tendon and muscle properties presented in Fig. 10.3. The solid lines correspond to the left hindlimb and the dashed lines correspond to the right hindlimb. The dotted blue lines in **c** indicate joint moments computed in the first stage optimization using as input experimental joint angles and EMG activity (see Eq. 10.10). The solid and dashed vertical lines indicate paw contact with the ground by the left and right hindlimbs, respectively. Positive moments are flexor for the ankle and hip and extensor for the knee. The experimental mean and SD values for the left mechanical variables were obtained from 5 cats (total number of cycles 61; cat 1 = 13, cat 2 = 10, cat 3 = 19, cat 4 = 11, cat 5 = 8)

The following cost function Z_3 was used for this optimization:

$$Z_3 = \frac{w_M}{6N} \sum_{j=1}^6 \sum_{t=1}^N \left[(M_{jt} - M_{jt}^e) / SD_j^M \right]^2 + \frac{w_F}{18N} \sum_{i=1}^{18} \sum_{t=1}^N \left[(F_{Mit} - A_{it}) / SD_j^u \right]^2 + \frac{w_a}{6N} \sum_{j=1}^6 \sum_{t=1}^N \left[(\theta_{jt} - \theta_{jt}^e) / SD_j^a \right]^2 + \frac{w_{FG}}{4N} \sum_{c=1}^4 \sum_{t=1}^N \left[(F_{Gct} - F_{Gct}^e) / SD_c^F \right]^2, \quad (10.13)$$

where M_{jt} , M_{jt}^e , F_{it} , A_{it} , SD_j^M and SD_j^u are the same as in Eq. (10.12) except here these variables were obtained for the two hindlimbs; subscripts $j=1,2,\dots,6$ in M_{jt} and M_{jt}^e and subscripts $i=1,2,\dots,18$ in F_{it} and A_{it} designate joints and muscles, respectively, in two hindlimbs; θ_{jt} and θ_{jt}^e are computed and experimental joint angles at the j -th joint of two hindlimbs at the t -th time frame, subscripts $j=1,2,\dots,6$ designate hip, knee and ankle joints of two hindlimbs; F_{Gct} and F_{Gct}^e are computed and experimental ground reaction forces, subscripts $c=1,2,\dots,4$ designate anterior-posterior and vertical components of ground reaction forces applied to two hindlimbs; SD_j^a and SD_c^F are the experimental standard deviations of j -th joint angle and c -th ground reaction force component; $w_M=1$; $w_F=1$; $w_a=10$; and $w_{FG}=10$.

EMG linear envelopes obtained for 9 muscles of one hindlimb were used as input to each muscle of the model assuming symmetry between the two hindlimbs. The initial conditions for integration of equations of hindlimb and muscle dynamics—the generalized segment positions and velocities as well as MTU lengths and velocities at swing onset of the left hindlimb—were determined experimentally as described above. The equations of hindlimb and muscle dynamics also served as constraints for the optimization problem.

The found optimal solution allowed a relatively close match between computed and experimental hip joint angle, two components of the ground reaction forces and resultant muscle moments at the joints (Fig. 10.5). However, there were rather large discrepancies in the computed knee joint angles during the swing phase (up to 40°) and in the ankle joint angles during stance, Fig. 10.5a). Since our goal was to evaluate length and velocity dependent afferent feedback from muscles based on muscle fascicle length and velocity, computed in turn from joint kinematics, such large errors were considered unacceptable.

Although we were not able to determine the exact reasons for the inability of our model to fit the experimental data more closely, the examination of previous publications that demonstrated better fits (e.g. (Neptune et al. 2009)) suggested that possible inaccuracies in our computations could result from Eqs. (10.7) and (10.8) describing the tendon force-length and contractile element force-velocity relations, as well as the force-length relation for the contractile element consisting of a set of straight lines (see above). The description of the tendon and muscle properties in our model contained discontinuities in the derivatives of force over length and velocity that appeared to be the major distinct feature of our model. These discontinuities did not cause visible problems during simulations of force production during isovelocity MTU ramps of the fully activated SO (Fig. 10.4), but could potentially

cause the observed large deviations in knee and ankle angles when MTU lengths changed with variable velocity at alternating muscle activation.

We therefore substituted the force-length relations for the tendon and parallel elastic element, as well as the force-length and force-velocity relations for the muscle contractile element with more conventional ones that are typically used in musculoskeletal modeling and are smooth (e.g., (Markin et al. 2010)). These equations are presented in Table 10.3. Parameters of these equations F_M^{\max} , L_{T0} , a_1 and a_2 were again optimized for each muscle, whereas parameters k_{T2} and ρ were optimized for two groups of muscles and considered the same within each group—muscles with a relatively short ($L_{T0}/L_{M0} \leq 1$) and long ($L_{T0}/L_{M0} > 1$) relative tendon length (as identified in the literature, (Sacks and Roy 1982), Tables 10.2 and 10.3). These parameters were tuned by minimizing the cost function Z_2 (Eq. 10.12), i.e. minimizing the difference between simulated and experimental resultant joint moments and between simulated normalized muscle forces and activation using the experimentally obtained mean muscle activity (Fig. 10.2b) and joint angles (Fig. 10.5a) as input. The tuned muscle parameters (Table 10.3) produced a close match with the experimental joint moments during the walking cycle (Fig. 10.6c, blue dotted lines).

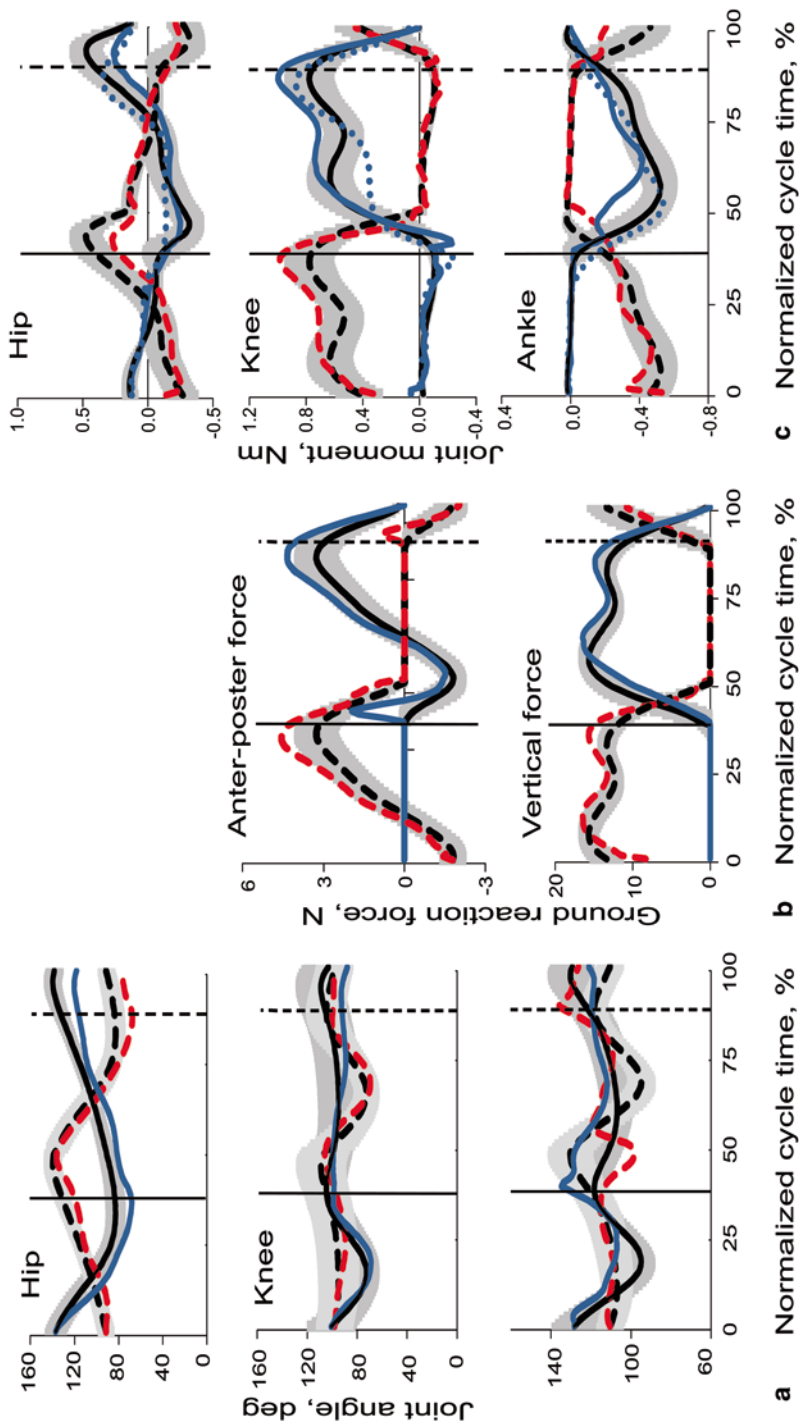
The parameters of viscoelastic interactions with the environment, constant forward velocity of the distal trunk endpoint and constants τ_{act} and τ_{deact} were tuned by minimizing cost function Z_3 (Eq. 10.13) while all other muscle parameters were fixed. The results of this optimization demonstrated a much better fit between simulated and experimental joint angles, ground reaction forces and joint moments (Fig. 10.6)—in most cases the simulated variables were within one standard deviation of the experimental ones.

10.2.2.4 Computation of Motion-Dependent Afferent Feedback

Computed muscle fiber length and velocity, and tendon force for each muscle during walking were used to estimate the firing rates of the corresponding muscle afferents. Muscle length-dependent afferent signals, the firing rates of muscle Ia and II spindle afferents, were calculated as functions of muscle fascicle length, velocity and muscle activity using the modified regression equations developed by (Prochazka and Gorassini 1998b; Prochazka 1999). These authors developed the equations based on their measurements of the firing rates of group Ia and II spindle afferents and MTU lengths in walking cats and on earlier similar models (e.g. (Houk et al. 1981)). To compute the firing rate of Ib Golgi tendon afferents, we assumed the Ib activity being proportional to muscle force during the mid-range of forces (see for example (Houk et al. 1981; Crago et al. 1982)). The Ia, II and Ib activity was computed as follows:

$$R_{Ia} = 4.3V_M^{0.6} + 2\Delta L_M + 100k_u^{\max}u + R_{Ia_0}, \quad (10.14)$$

$$R_{II} = 13.5\Delta L_M + 20u + R_{II_0}, \quad (10.15)$$



a Normalized cycle time, % **b** Normalized cycle time, % **c** Normalized cycle time, %

Fig. 10.6 Recorded mean (black lines) \pm SD (gray shadow) and computed (blue and red lines) joint angles **a**, ground reaction forces **b** and joint moments **c** for two hindlimbs during a cycle of walking. Simulations were based on the tendon and muscle properties presented in Tables 10.2 and 10.3. For other information see the legend for Fig. 10.5

$$R_{Ib} = k_{Ib} F_M / F_M^{Max}, \quad (10.16)$$

where R_{Ia} , R_{II} and R_{Ib} are the firing rates of spindle primary and secondary afferents and Golgi tendon organ afferents (imp/s), respectively; V_M is muscle (fascicle) velocity (mm/s); ΔL_M is muscle length change from the mean value in a cycle (mm); F_M / F_M^{Max} is normalized muscle force; u , normalized rectified and low-pass filtered EMG activity (Fig. 10.2b); k_{Ib} is the firing rate of Ib afferents per unit of normalized muscle force ($k_{Ib} = 333$ imp/s, (Prochazka 1999)); R_{Ia_0} and R_{II_0} are the mean firing rates of Ia and II afferents in a walking cycle (see Table 10.2).

In addition, the firing rate of cutaneous afferents from the plantar surface of the paw was calculated as a function of the vertical ground reaction force and the positive rate of its change during stance:

$$R_c = k_{c1} (F_{Gy} + k_{c2} \dot{F}_{Gy}), \quad (10.17)$$

where R_c is the firing rate of cutaneous afferents from paw pad (imp/s), $k_{c1} = 1$, and $k_{c2} = \begin{cases} 160, & \text{if } \dot{F}_y > 0 \\ 0, & \text{if } \dot{F}_y \leq 0 \end{cases}$. The equation was derived based on recordings of cutaneous afferent activity and simulated ground reaction forces (see above).

10.3 Comparison of Simulated and Experimental Walking Mechanics and Afferent Activity

10.3.1 Input to the Simulation Model—EMG Patterns

Patterns of EMG activity of major hindlimb muscles obtained in this study for individual animals (Fig. 10.2a) and EMG envelopes averaged across 5 cats (Fig. 10.2b) were consistent with previous reports (e.g., (Smith et al. 1998; Krouchev et al. 2006; Markin et al. 2012)). Specifically, major hindlimb extensors (SO, GA, VA, BFA) were active primarily during stance, whereas flexors (TA, SAM, IP) were active mostly during swing. Two-joint thigh muscles with flexion and extension function at two joints (RF, BFP) were active close to or at the swing-stance and stance-swing transitions.

Averaged EMG pattern of each muscle normalized to a cycle time (Fig. 10.2b) was locally fitted by a cubic spline function and EMG values were calculated at each 0.075-ms time step. These re-sampled EMG patterns (with the initial positions and velocities of the generalized coordinates determined experimentally) were used as input to the model. Muscle activation was computed first (Eq. 10.6), followed by muscle and tendon forces (Eqs. 10.4–10.5), and tendon acceleration of each

muscle (Eq. 10.3); finally muscle and limb dynamics were computed by integrating Eqs. (10.3) and (10.2).

10.3.2 *Walking Kinematics and Kinetics*

The mean patterns of joint angles, ground reaction forces and joint moments during level overground walking in the cat obtained experimentally here (Figs. 10.5 and 10.6, thin black lines) were consistent with previously published results (Manter 1938; Lavoie et al. 1995; Prilutsky et al. 2005; Gregor et al. 2006).

Identified model parameters (see above) and parameters taken from the literature or measured in this study (Tables 10.1–10.3) allowed for a close match between simulated walking mechanics and the corresponding mean mechanical variables obtained experimentally—the computed variables were typically within one standard deviation from the experimental ones (Fig. 10.6). It should be pointed out that in the obtained forward dynamics solution the passive joint moments at the hip, knee and ankle (vector \mathbf{S} in Eq. 10.2) were not engaged because computed joint angles were within normal locomotor ranges (see Sect. 10.2.2.1).

The average speed of simulated walking was 0.505 m/s, whereas the average experimental speed of 5 animals was 0.646 m/s. Among three joint angles, the computed hip and knee angles corresponded to the mean patterns of the 5 cats with slight deviation from them at the transition from swing to stance or in early stance, but were within or close to one SD of the mean experimental values (Fig. 10.6a). The computed ankle angle was typically within or close to one SD of the mean recorded angle during swing and most of stance, but deviated substantially from the mean pattern in early and terminal stance (Fig. 10.6a). This difference could have resulted from modeling the foot as a rigid segment, whereas it consists of the tarsals and digits (paw). Overall, however, the computed joint angles were essentially within one SD from the mean experimental values and thus could be considered satisfactory.

The computed joint moments generally reproduced the mean experimental patterns (Fig. 10.6c). For example, during stance, the computed ankle and knee moments were extensor and reproduced well general experimental patterns, although the computed ankle moments deviated from the mean experimental values in early stance by more than one SD; the computed knee moments in mid stance were slightly higher than the mean+SD of experimental moments. The hip moments were generally within one SD from the mean experimental moments, being extensor in first half of stance and flexor in the second half, although were slightly lower than the mean-SD in terminal stance. Generally similar results were obtained during the stage 2 optimization performed to identify muscle model parameters using as input experimentally recorded joint angles and muscle activity (see Eq. 10.12 and Fig. 10.6c, blue dotted line).

During optimization (Eqs. 10.12 and 10.13), it was assumed that muscle active state A provides the greatest contribution to muscle force F_M (Eq. 10.5) and thus the

force-length $F_{CE}(L_M)$ and force-velocity $F_{CE}(V_M)$ properties of the contractile element do not substantially affect muscle force during walking. This assumption is supported by a very high correlation ($r^2 > 0.9$) between the muscle force and the low-pass filtered EMG, shifted in time to account for the excitation-activation coupling, synchronously recorded during cat walking from the same muscle—soleus (Norman et al. 1988; Liu et al. 1999) and plantaris (Herzog et al. 1998). Another evidence for a relatively small contribution of the CE force-length-velocity properties to the muscle force during gait was obtained by (Davy and Audu 1987; Anderson and Pandy 2001) who compared computed muscle forces during human walking with and without inclusion of the contractile muscle properties in their models—both calculations gave similar results.

The anterior-posterior and vertical ground reaction forces computed using the model likewise closely matched the mean experimental patterns except short phases at foot contact for the horizontal forces; Fig. 10.6b).

10.3.3 Computed Activity of Muscle and Cutaneous Afferents During Walking

The computed firing rates of selected afferents could be compared with the corresponding rates recorded *in vivo* in walking cats (Loeb and Duysens 1979; Loeb 1981; Loeb et al. 1985; Prochazka and Gorassini 1998a, b; Weber et al. 2007). This comparison can be considered a model validation test because the model parameters were not tuned to match experimental patterns of afferent activity. It should be noted that the regression equations for computing activity of spindle Ia and II afferents (Eqs. 10.14 and 10.15) were based on measurements of MTU length as an independent variable (Prochazka and Gorassini 1998a, b). Therefore, derivations of the firing rates of spindle afferents from MTU lengths for muscles with a very large ratio L_{T0}/L_0 , as in GA (Table 10.3), may be less accurate than those derived for muscles with a small L_{T0}/L_0 ratio, as in BFP or SAM (Table 10.3) because a substantial part of MTU length changes in muscles like GA can be taken up by the long tendon (Hoffer et al. 1989; Maas et al. 2009) rather than by muscle fascicles and thus the spindles. The maximum correlation coefficients computed between measured and predicted firing rates of group Ia and II afferents from cat triceps surae ($r^2 = 0.62 - 0.73$) were in fact lower than those for hamstrings ($r^2 = 0.942 - 0.80$) (Prochazka and Gorassini 1998a, b).

The comparison of computed activity of muscle length-dependent type Ia and II afferents with the corresponding measured activity for BFP, VA, RF and SAM afferents showed reasonable qualitative agreement (Fig. 10.7a, b). Specifically, the computed and recorded type Ia and II BFP afferents increase their activity from mid swing reaching a peak near the paw contact; the activity subsided during stance with a slight rising of Ia activity in terminal stance. Type Ia VA afferent activity had two peaks—in late stance—early swing and in mid stance—and low or

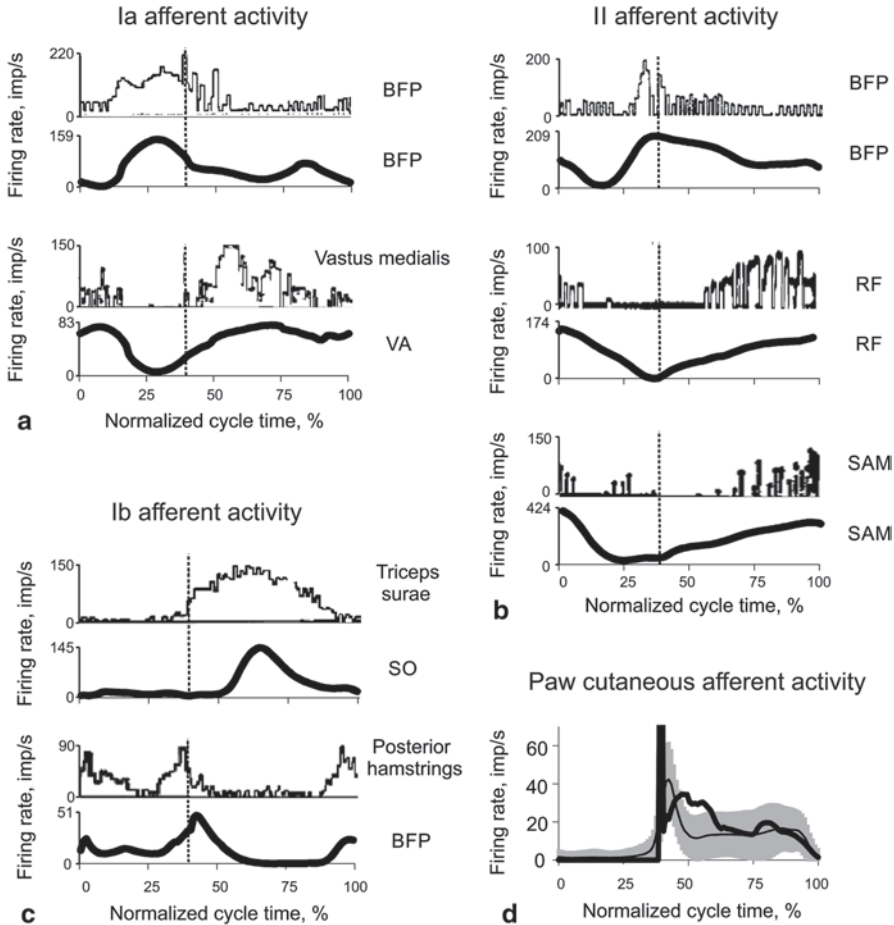


Fig. 10.7 Comparison of computed (*thick lines*) and recorded *in vivo* (*thin lines*) firing rates of group Ia **a**, II **b** and Ib **c** afferents from selected muscles and cutaneous paw pad afferents **d** during the walking cycle (see text for explanations). The *vertical dotted lines* separate the swing and stance phases. Muscle abbreviations are the same as in Fig. 10.1c. *In vivo* activities of muscle afferents are reproduced with permission from: Ia biceps femoris posterior (BFP) and II BFP—Fig. 2 from (Loeb and Duysens 1979), American Physiological Society; Ia vastus medialis—Fig. 3 from (Loeb et al. 1985), American Physiological Society; spindle afferent from rectus femoris (RF)—Fig. 5 from (Loeb 1981), © Canadian Science Publishing, assumed to be spindle secondary afferent; sartorius medial (SAM)—Fig. 6 from (Loeb et al. 1985), American Physiological Society; Ib triceps surae and Ib posterior hamstrings—Fig. 6 (Prochazka and Gorassini 1998a), John Wiley and Sons. The mean (*thin line*) \pm SD (*gray shadow*) activity of paw afferents in **d** is obtained from recorded 4 afferents of one animal collected during 11 walking cycles

zero activity during the second half of swing. The absolute peak values of computed firing rates of these afferents deferred substantially—up to 43% (Fig. 10.7a, Ia VA). The computed patterns of group II afferents from RF and SAM were also in qualitative agreement with the measured activity, both increasing from early stance to the peak activity at terminal stance and early swing (Fig. 10.7b). The peak values of the firing rates, however, differed substantially between calculations and measurements.

The computed firing rate of Ib afferents from SO and BFP also demonstrated patterns qualitatively similar to those of recorded afferents (Fig. 10.7c). For instance, Ib SO afferents were mostly active during stance with very little activity during swing, whereas Ib BFP activity occurred at the stance-swing and swing-stance transitions. The difference in absolute peak values between the computed and recorded Ib activity was small for SO and substantial for BFP Ib afferents.

The instantaneous firing rate of cutaneous paw pad afferents computed as a function of the vertical ground reaction force and its time derivative (Eq. 10.17) demonstrated a sharp peak at paw contact and the moderate magnitude during the rest of stance, similar to the recorded activity of mechanoreceptors from paw pad (Fig. 10.7d). Constants k_{c1} and k_{c2} in Eq. 10.17 were selected to match the mean recorded firing rate values.

Given the reasonable qualitative agreement between patterns of the computed and recorded activity of type Ia, Ib and II afferents from selected muscles, as well as of paw pad afferents, the developed model can be integrated with a CPG model (Rybak et al. 2006a, b) and used for a closed-loop simulations and computational studies of spinal locomotion (see chapter by (Markin et al. 2015)). These simulations have the potential to provide additional more detailed information compared to the previous similar simulations (Ivashko et al. 2003; Markin et al. 2010) because the CPG model and the musculoskeletal model reasonably reproduce the activity patterns in fictive locomotion (Rybak et al. 2006a, b) and mechanics (Fig. 10.6) and afferent activity (Fig. 10.7) during real cat walking.

In addition, the developed musculoskeletal model provides patterns of type Ia, Ib and II muscle and paw pad cutaneous afferent activities during cat locomotion (Figs. 10.7 and 10.8). This information has not been available in such detail and can be used for investigating the role of different types of afferents in modulating muscle activity and controlling phase transitions. The results presented in Figs. 10.7 and 10.8 suggest that type II afferents from hip flexors IP, RF and SAM may trigger the extensor-flexor phase transition (or stance-swing transition) as their maximum activity is reached at terminal stance, while load sensitive afferents (type Ib from extensor muscles—SO, GA, VA and BFA and cutaneous paw receptors) approach their minimum activity at that time. This conclusion is consistent with earlier similar suggestions (Ekeberg and Pearson 2005; Pearson 2008). Type Ia and II afferents from BFP and TA as well as type Ia afferents from IP, RF and SAM could participate in controlling the flexor-extensor phase transition (or swing-stance transition), since these afferents reach their maximum activity at terminal swing (Fig. 10.8).

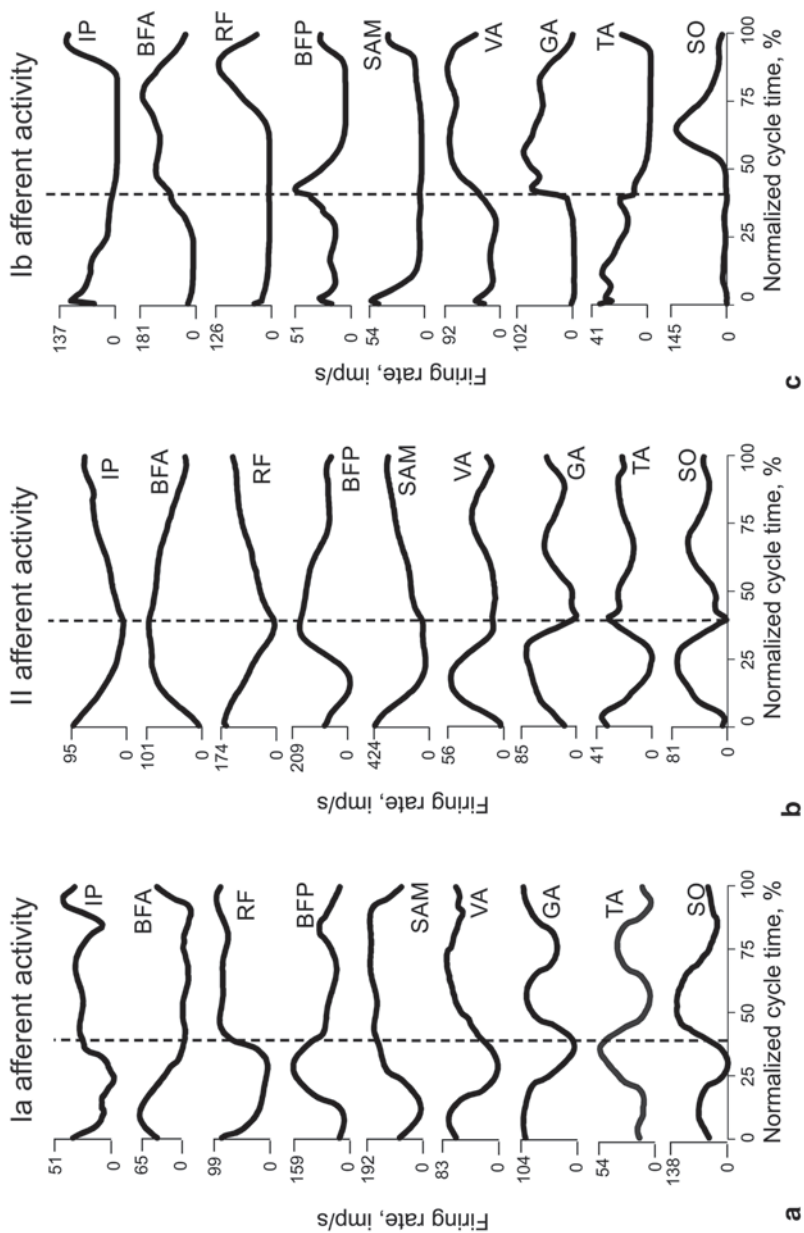


Fig. 10.8 Computed type Ia **a**, II **b**, and Ib **c** afferent activities from 9 hindlimb muscles in the walking cycle. The vertical dashed lines separate the swing and stance phases. For muscle abbreviations see legends in Fig. 10.1c

10.4 Limitations of the Model

Although the forward dynamics model developed in this study reproduces reasonably well cat walking mechanics (Fig. 10.6) and activity of selected afferents (Fig. 10.7) using recorded EMG patterns of hindlimb muscles as input, several limitations of the model should be pointed out. First, it was assumed that the instantaneous muscle fiber velocity, length and force (and EMG magnitude in case of Ia afferents) uniquely determine the afferent activity. This assumption is difficult to verify. Simultaneous recordings from primary and secondary afferents and MTU length and force information during cat locomotion have been conducted in limited studies and in some instances revealed relatively low correlations between ensemble afferent activity and the corresponding mechanical variables (Loeb et al. 1985; Prochazka and Gorassini 1998a) especially for muscles with short fascicles and long tendons (i.e. gastrocnemius) in which fascicle (and thus spindle) length changes may differ from the recorded MTU length changes (Hoffer et al. 1989; Maas et al. 2009). The potential impact of compliant MTUs on the computed length-dependent afferent activity was reduced in the present model by accounting for tendon deformation.

Secondly, the employed models for computing muscle afferent signals (Eqs. 10.14–10.17) have been maximally simplified to enable online computations of afferent signals in the combined model of the CPG and musculoskeletal system (e.g. (Ivashko et al. 2003; Markin et al. 2010, 2015)). More accurate transfer functions relating muscle mechanical state with afferent activity (Houk et al. 1981; Prochazka 1999) or highly detailed models of the spindle and Golgi tendon receptors (e.g. (Mileusnic et al. 2006; Mileusnic and Loeb 2006)) would be difficult to implement in the online computations of afferent input.

Furthermore, the joint mechanoreceptor activities were not included in the current model, although they may affect the functional organization of spinal circuits (Rudomin et al. 2007). However, these afferents are mostly active at extreme joint positions (Ferrell 1980) which were not reached in the obtained forward dynamics simulation (Fig. 10.6a). This type of afferent information could be incorporated into the neuromechanical model of spinal control of locomotion in the future.

Finally, the model seems able to reproduce only pattern of changes in afferent activity rather than the absolute firing rate values. The impact of this limitation may be reduced by, for example, finding appropriate gains of the feedback signals in a combined closed-loop neuromechanical model that would permit a proper transformation of fictive locomotor activity patterns generated by the CPG model (Rybak et al. 2006b) to the EMG patterns of normal walking (Fig. 10.2); see (Markin et al. 2015).

Acknowledgements This work was supported by NIH grants HD-032571, NS-048844, and EB012855 and by the Center for Human Movement Studies at Georgia Institute of Technology. We would like to thank Dr. Guayhaur Shoe for his technical assistance.

References

- Akay T, Tourtellotte WG, Arber S, Jessell TM (2014) Degradation of mouse locomotor pattern in the absence of proprioceptive sensory feedback. *Proc Natl Acad Sci U S A* 111:16877–16882
- Anderson FC, Pandy MG (2001) Static and dynamic optimization solutions for gait are practically equivalent. *J Biomech* 34:153–161
- Aoi S (2015) Neuromusculoskeletal modeling for the adaptive control of posture during locomotion. In: Prilutsky BI, Edwards DH Jr (eds) *Neuromechanical modeling of posture and locomotion*. Springer, New York (in press)
- Aoi S, Kondo T, Hayashi N, Yanagihara D, Aoki S, Yamaura H et al (2013) Contributions of phase resetting and interlimb coordination to the adaptive control of hindlimb obstacle avoidance during locomotion in rats: a simulation study. *Biol Cybern* 107:201–216
- Ariano MA, Armstrong RB, Edgerton VR (1973) Hindlimb muscle fiber populations of five mammals. *J Histochem Cytochem* 21:51–55
- Baratta RV, Solomonow M, Best R, Zembo M, D'Ambrosia R (1995) Architecture-based force-velocity models of load-moving skeletal muscles. *Clin Biomech (Bristol Avon)* 10:149–155
- Bondy B, Klishko AN, Prilutsky BI, Cymbalyuk G (2015) Control of cat walking and paw-shake by a multifunctional central pattern generator. In: Prilutsky BI, Edwards DH (eds) *Neuromechanical modeling of posture and locomotion*. Springer, New York (in press)
- Brown TG (1914) On the nature of the fundamental activity of the nervous centres; together with an analysis of the conditioning of rhythmic activity in progression, and a theory of the evolution of function in the nervous system. *J Physiol* 48:18–46
- Brown IE, Liinamaa TL, Loeb GE (1996a) Relationships between range of motion, lo, and passive force in five strap-like muscles of the feline hind limb. *J Morphol* 230:69–77
- Brown IE, Scott SH, Loeb GE (1996b) Mechanics of feline soleus: II. Design and validation of a mathematical model. *J Muscle Res Cell Motil* 17:221–233
- Bunderson N, Bingham J (2015) Better science through predictive modeling: numerical tools for understanding neuromechanical interactions. In: Prilutsky BI, Edwards DH Jr (eds) *Neuromechanical modeling of posture and locomotion*. Springer, New York (in press)
- Bunderson NE, Bingham JT, Sohn MH, Ting LH, Burkholder TJ (2012) Neuromechanic: a computational platform for simulation and analysis of the neural control of movement. *Int J Numer Method Biomed Eng* 28:1015–1027
- Conway BA, Hultborn H, Kiehn O (1987) Proprioceptive input resets central locomotor rhythm in the spinal cat. *Exp Brain Res* 68:643–656
- Corana A, Marchesi M, Martini C, Ridella S (1987) Minimizing multimodal functions of continuous variables with the “simulated annealing” algorithm. *ACM Trans Math Softw* 13:263–280
- Crago PE, Houk JC, Rymer WZ (1982) Sampling of total muscle force by tendon organs. *J Neurophysiol* 47:1069–1083
- Davy DT, Audu ML (1987) A dynamic optimization technique for predicting muscle forces in the swing phase of gait. *J Biomech* 20:187–201
- De Groot F, Van Campen A, Jonkers I, De Schutter J (2010) Sensitivity of dynamic simulations of gait and dynamometer experiments to hill muscle model parameters of knee flexors and extensors. *J Biomech* 43:1876–1883
- Duysens J, Loeb GE (1980) Modulation of ipsi- and contralateral reflex responses in unrestrained walking cats. *J Neurophysiol* 44:1024–1037
- Edman KA (1988) Double-hyperbolic force-velocity relation in frog muscle fibres. *J Physiol* 404:301–321
- Ekeberg O, Pearson K (2005) Computer simulation of stepping in the hind legs of the cat: an examination of mechanisms regulating the stance-to-swing transition. *J Neurophysiol* 94:4256–4268
- Ferrell WR (1980) The adequacy of stretch receptors in the cat knee joint for signalling joint angle throughout a full range of movement. *J Physiol* 299:85–99
- Gareis H, Solomonow M, Baratta R, Best R, D'Ambrosia R (1992) The isometric length-force models of nine different skeletal muscles. *J Biomech* 25:903–916

- Gordon AM, Huxley AF, Julian FJ (1966) The variation in isometric tension with sarcomere length in vertebrate muscle fibres. *J Physiol* 184:170–192
- Gregor RJ, Smith DW, Prilutsky BI (2006) Mechanics of slope walking in the cat: quantification of muscle load, length change, and ankle extensor EMG patterns. *J Neurophysiol* 95:1397–1409
- Grillner S (1981) Control of locomotion in bipeds, tetrapods, and fish. In: Brooks V (ed) *Handbook of physiology. Section I. The nervous system, vol II.* American Physiological Society, Bethesda, pp 1179–1236
- Grillner S, Georgopoulos AP, Jordan LM (1999) Selection and initiation of motor behavior. In: Stein PSG, Grillner S, Selverston AI, Stuart DG (eds) *Neurons, networks, and motor behavior.* MIT, Boston, pp 3–19
- Guertin P, Angel MJ, Perreault MC, McCrea DA (1995) Ankle extensor group I afferents excite extensors throughout the hindlimb during fictive locomotion in the cat. *J Physiol* 487(Pt 1):197–209
- He J, Levine WS, Loeb GE (1991) Feedback gains for correcting small perturbations to standing posture. *IEEE Trans Autom Control* 36:322–332
- Herzog W, Sokolosky J, Zhang YT, Guimaraes AC (1998) EMG-force relation in dynamically contracting cat plantaris muscle. *J Electromyogr Kinesiol* 8:147–155
- Hill AV (1938) The heat of shortening and the dynamic constants of muscle. *Proc Royal Soc (Lond) B* 126:136–95
- Hoffer JA, Caputi AA, Pose IE, Griffiths RI (1989) Roles of muscle activity and load on the relationship between muscle spindle length and whole muscle length in the freely walking cat. *Prog Brain Res* 80:75–85; discussion 57–60
- Houk JC, Rymer WZ, Crago PE (1981) Dependence of dynamic response of spindle receptors on muscle length and velocity. *J Neurophysiol* 46:143–166
- Hoy MG, Zernicke RF (1985) Modulation of limb dynamics in the swing phase of locomotion. *J Biomech* 18:49–60
- Ivashko DG, Prilutsky BI, Markin SN, Chapin JK, Rybak IA (2003) Modeling the spinal cord neural circuitry controlling cat hindlimb movement during locomotion. *Neurocomputing* 52–54:621–629
- Jordan LM (1998) Initiation of locomotion in mammals. *Ann N Y Acad Sci* 860:83–93
- Kiehn O (2011) Development and functional organization of spinal locomotor circuits. *Curr Opin Neurobiol* 21:100–109
- Krouchev N, Kalaska JF, Drew T (2006) Sequential activation of muscle synergies during locomotion in the intact cat as revealed by cluster analysis and direct decomposition. *J Neurophysiol* 96:1991–2010
- Lavoie S, McFadyen B, Drew T (1995) A kinematic and kinetic analysis of locomotion during voluntary gait modification in the cat. *Exp Brain Res* 106:39–56
- Liu MM, Herzog W, Savelberg HH (1999) Dynamic muscle force predictions from EMG: an artificial neural network approach. *J Electromyogr Kinesiol* 9:391–400
- Loeb GE (1981) Somatosensory unit input to the spinal cord during normal walking. *Can J Physiol Pharmacol* 59:627–635
- Loeb GE, Dyuysens J (1979) Activity patterns in individual hindlimb primary and secondary muscle spindle afferents during normal movements in unrestrained cats. *J Neurophysiol* 42:420–440
- Loeb GE, Hoffer JA, Pratt CA (1985) Activity of spindle afferents from cat anterior thigh muscles. I. Identification and patterns during normal locomotion. *J Neurophysiol* 54:549–564
- Maas H, Gregor RJ, Hodson-Tole EF, Farrell BJ, Prilutsky BI (2009) Distinct muscle fascicle length changes in feline medial gastrocnemius and soleus muscles during slope walking. *J Appl Physiol* 106:1169–1180
- Manter JT (1938) The dynamics of quadrupedal walking. *J Exp Biol* 15:522–540
- Markin SN, Klishko AN, Shevtsova NA, Lemay MA, Prilutsky BI, Rybak IA (2010) Afferent control of locomotor CPG: insights from a simple neuromechanical model. *Ann N Y Acad Sci* 1198:21–34

- Markin SN, Lemay MA, Prilutsky BI, Rybak IA (2012) Motoneuronal and muscle synergies involved in cat hindlimb control during fictive and real locomotion: a comparison study. *J Neurophysiol* 107:2057–2071
- Markin SN, Klishko AN, Shevtsova NA, Lemay MA, Prilutsky BI, Rybak IA (2015) A neuro-mechanical model of spinal control of locomotion. In: Prilutsky BI, Edwards DH Jr (eds) *Neuromechanical modeling of posture and locomotion*. Springer, New York (in press)
- McCrea DA (2001) Spinal circuitry of sensorimotor control of locomotion. *J Physiol* 533:41–50
- McCrea DA, Rybak IA (2008) Organization of mammalian locomotor rhythm and pattern generation. *Brain Res Rev* 57:134–146
- Mileusnic MP, Loeb GE (2006) Mathematical models of proprioceptors. II. Structure and function of the Golgi tendon organ. *J Neurophysiol* 96:1789–1802
- Mileusnic MP, Brown IE, Lan N, Loeb GE (2006) Mathematical models of proprioceptors. I. Control and transduction in the muscle spindle. *J Neurophysiol* 96:1772–1788
- Neptune RR, McGowan CP, Kautz SA (2009) Forward dynamics simulations provide insight into muscle mechanical work during human locomotion. *Exerc Sport Sci Rev* 37:203–210
- Norman R, Gregor RJ, Dowling J (1988) The prediction of cat tendon force from EMG in dynamic muscular contractions. In: Cotton CE, Lamontagne M, Robertson DGE et al (eds) *Biennial Conference of Canadian Society for Biomechanics*. SPODYN, London, Ontario, pp 120–121
- Orlovsky GN, Deliagina TG, Grillner S (1999) *Neuronal control of locomotion: from mollusc to man*. Oxford University Press, New York
- Pearson KG (2008) Role of sensory feedback in the control of stance duration in walking cats. *Brain Res Rev* 57:222–227
- Pearson KG, Collins DF (1993) Reversal of the influence of group Ib afferents from plantaris on activity in medial gastrocnemius muscle during locomotor activity. *J Neurophysiol* 70:1009–1017
- Prilutsky BI, Klishko AN (2007) Activity of muscle spindle and tendon organ afferents during cat locomotion computed using a musculoskeletal model. In: *Society for Neuroscience Meeting*. Program No. 189.14. 2007 Neuroscience Meeting Planner. Online, San Diego, CA
- Prilutsky BI, Herzog W, Leonard TR, Allinger TL (1996) Role of the muscle belly and tendon of soleus, gastrocnemius, and plantaris in mechanical energy absorption and generation during cat locomotion. *J Biomech* 29:417–434
- Prilutsky BI, Sirota MG, Gregor RJ, Beloozerova IN (2005) Quantification of motor cortex activity and full-body biomechanics during unconstrained locomotion. *J Neurophysiol* 94:2959–2969
- Prilutsky BI, Maas H, Bulgakova M, Hodson-Tole EF, Gregor RJ (2011) Short-term motor compensations to denervation of feline soleus and lateral gastrocnemius result in preservation of ankle mechanical output during locomotion. *Cells Tissues Organs* 193:310–324
- Prilutsky BI, Klishko AN, Weber DJ, Lemay MA (2013) Activity of muscle and paw-skin afferents during cat locomotion computed using a forward dynamics neuromechanical model. In: *XXIV Congress of International Society of Biomechanics*. 2013. Natal, Brazil
- Prochazka A (1999) Quantifying proprioception. *Prog Brain Res* 123:133–142
- Prochazka A, Gorassini M (1998a) Ensemble firing of muscle afferents recorded during normal locomotion in cats. *J Physiol* 507(Pt 1):293–304
- Prochazka A, Gorassini M (1998b) Models of ensemble firing of muscle spindle afferents recorded during normal locomotion in cats. *J Physiol* 507(Pt 1):277–291
- Rossignol S (2006) Plasticity of connections underlying locomotor recovery after central and/or peripheral lesions in the adult mammals. *Philos Trans R Soc Lond B Biol Sci* 361:1647–1671
- Rudomin P, Hernandez E, Lomeli J (2007) Tonic and phasic differential GABAergic inhibition of synaptic actions of joint afferents in the cat. *Exp Brain Res* 176:98–118
- Rybak IA, Shevtsova NA, Lafreniere-Roula M, McCrea DA (2006a) Modelling spinal circuitry involved in locomotor pattern generation: insights from deletions during fictive locomotion. *J Physiol* 577:617–639
- Rybak IA, Stecina K, Shevtsova NA, McCrea DA (2006b) Modelling spinal circuitry involved in locomotor pattern generation: insights from the effects of afferent stimulation. *J Physiol* 577:641–658

- Sacks RD, Roy RR (1982) Architecture of the hind limb muscles of cats: functional significance. *J Morphol* 173:185–195
- Sandercock TG, Heckman CJ (1997) Force from cat soleus muscle during imposed locomotor-like movements: experimental data versus Hill-type model predictions. *J Neurophysiol* 77:1538–1552
- Scott SH, Loeb GE (1995) Mechanical properties of aponeurosis and tendon of the cat soleus muscle during whole-muscle isometric contractions. *J Morphol* 224:73–86
- Scovil CY, Ronsky JL (2006) Sensitivity of a Hill-based muscle model to perturbations in model parameters. *J Biomech* 39:2055–2063
- Shik ML, Severin FV, Orlovsky GN (1969) Control of walking and running by means of electrical stimulation of the mesencephalon. *Electroencephalogr Clin Neurophysiol* 26:549
- Shoham S, Fellows MR, Normann RA (2003) Robust, automatic spike sorting using mixtures of multivariate t-distributions. *J Neurosci Methods* 127:111–122
- Siebert T, Rode C, Herzog W, Till O, Blickhan R (2008) Nonlinearities make a difference: comparison of two common Hill-type models with real muscle. *Biol Cybern* 98:133–143
- Smith JL, Carlson-Kuhta P, Trank TV (1998) Forms of forward quadrupedal locomotion. III. A comparison of posture, hindlimb kinematics, and motor patterns for downslope and level walking. *J Neurophysiol* 79:1702–1716
- Spector SA, Gardiner PF, Zernicke RF, Roy RR, Edgerton VR (1980) Muscle architecture and force-velocity characteristics of cat soleus and medial gastrocnemius: implications for motor control. *J Neurophysiol* 44:951–960
- Takeoka A, Vollenweider I, Courtine G, Arber S (2014) Muscle spindle feedback directs locomotor recovery and circuit reorganization after spinal cord injury. *Cell* 159:1626–1639
- van den Bogert AJ, Schamhardt HC, Crowe A (1989) Simulation of quadrupedal locomotion using a rigid body model. *J Biomech* 22:33–41
- Weber DJ, Stein RB, Everaert DG, Prochazka A (2007) Limb-state feedback from ensembles of simultaneously recorded dorsal root ganglion neurons. *J Neural Eng* 4:S168–S180
- Whelan PJ, Hiebert GW, Pearson KG (1995) Stimulation of the group I extensor afferents prolongs the stance phase in walking cats. *Exp Brain Res* 103:20–30
- Yakovenko S, Gritsenko V, Prochazka A (2004) Contribution of stretch reflexes to locomotor control: a modeling study. *Biol Cybern* 90:146–155
- Zajac FE (1989) Muscle and tendon: properties, models, scaling, and application to biomechanics and motor control. *Crit Rev Biomed Eng* 17:359–411